Agricultural and Forest Meteorology 378 (2026) 110960

Contents lists available at ScienceDirect

Agricultural and Forest Meteorology

journal homepage: www.elsevier.com/locate/agrformet

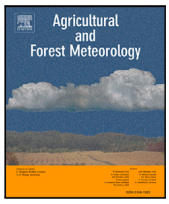

Beyond surface fluxes: Observational and computational needs of multilayer canopy models – A walnut orchard test case

Gordon B. Bonan [a,*], Sean P. Burns [a,b], Edward G. Patton [a]

[a] NSF National Center for Atmospheric Research, Boulder, CO, USA
[b] Department of Geography, University of Colorado, Boulder, CO, USA

ARTICLE INFO

Dataset link: github.com/gbonan, doi.org/10.5281/zenodo.17426258

Keywords:
Multilayer model
Canopy turbulence
Observation needs
Land surface model

ABSTRACT

Land surface models simulate fluxes exchanged between the land and atmosphere in weather and climate models. The prevailing modeling paradigm uses a big-leaf canopy parameterization that is not vertically-resolved. Multilayer canopy models have received interest over the past several years as a means to improve surface fluxes and enable new science. We present results from a comparison of the Community Land Model (CLM) multilayer canopy model (CLM-ml v2) and observations of air temperature, specific humidity, wind speed, and fluxes (net radiation, sensible heat, latent heat, momentum) at multiple heights in and above a walnut orchard during the Canopy Horizontal Array Turbulence Study (CHATS). The dataset provides a benchmark with which to test multilayer models. Above-canopy sensible heat, latent heat, and momentum fluxes are well simulated under a range of atmospheric regimes spanning strongly unstable, weakly unstable, near-neutral, weakly stable, and strongly stable, as are vertical profiles of fluxes within the canopy. Vertical profiles of wind speed closely match the observations under all stability regimes. Vertical profiles of air temperature and specific humidity are well simulated except for strongly stable conditions, when the first-order turbulence closure cannot represent within-canopy non-local vertical mixing that would otherwise transport the cool air produced by radiative cooling of the upper canopy downward to the lower canopy. Our model–data comparison highlights the potential of multilayer models to simulate the surface air space. The multilayer canopy model is simpler and more consistent with theory than is the CLM big-leaf canopy model, and it modernizes the canopy physics for theoretical and computational advances compared with CLM's outdated ad-hoc parameterizations. Nonetheless, our analysis points to further modeling needs and identifies observations central to model testing. Measurements of within-canopy micrometeorology and leaf gas exchange are needed in addition to above-canopy fluxes.

1. Introduction

Since the advent of land surface models for coupling with the atmosphere in weather and climate models, plant canopies have been modeled as a big-leaf without vertical structure (Deardorff, 1978; Dickinson et al., 1981, 1986; Sellers et al., 1986). An alternative was to model multiple layers in a vertically-resolved canopy (Cowan, 1968; Waggoner and Reifsnyder, 1968; Goudriaan and Waggoner, 1972; Shawcroft et al., 1974; Goudriaan, 1977). Big-leaf canopies were a rejection of multilayer canopies, which were deemed impractical (Raupach and Finnigan, 1988; Bonan et al., 2021).

There has been renewed interest in the use of multilayer canopies coupled to atmospheric models as theoretical advances, new datasets of leaf traits and canopy structure, and computational efficiency remove the impediments to model implementation (Bonan et al., 2021). A multilayer canopy has been developed for the ORCHIDEE land surface model (Chen et al., 2016; Ryder et al., 2016), and likewise for the Community Land Model (Bonan et al., 2018, 2021). Multilayer canopies have been implemented in the Weather Research and Forecasting model (Smallman et al., 2013; Falk et al., 2014; Xu et al., 2014) and in large eddy simulations (Patton et al., 2016; Ma and Liu, 2019; Pedruzo-Bagazgoitia et al., 2023). The JULES land surface model (Mercado et al., 2007; Wiltshire et al., 2020) and the FATES vegetation demography model (Koven et al., 2020) have a multilayer implementation of radiative transfer for photosynthesis and stomatal conductance, though not turbulent fluxes and scalar profiles.

Multilayer canopy models provide an opportunity to reconsider the parameterizations used in big-leaf land surface models. Version 5 of the Community Land Model (CLM5), for example, uses simplified ad-hoc

* Corresponding author.
E-mail address: bonan@ucar.edu (G.B. Bonan).

https://doi.org/10.1016/j.agrformet.2025.110960
Received 14 July 2025; Received in revised form 12 November 2025; Accepted 23 November 2025
Available online 2 December 2025

parameterizations of within-canopy turbulent processes that are 30–40 years old and date to the early origins of land surface models, and the latest version (CLM6) maintains these parameterizations (Lawrence et al., 2018). The fundamental framework to model plant canopies as a single layer of leaves with additional fluxes from the soil was put forth by Deardorff (1978), who formulated fluxes from the leaves to the canopy air, the soil to the canopy air, and the canopy air to the overlying atmosphere. Dickinson (1984) retained the framework, but modified some of the specifics of the model. His equations for wind speed in the canopy, under-canopy aerodynamics, and canopy air temperature are still used in CLM5/6.

Further rationale for multilayer canopy models is found in the benefit of forest microclimates for biological conservation. The cooler understory temperatures compared with the overstory or outside the forest in open fields help to mitigate the deleterious effects of hot temperatures on forest organisms (De Frenne et al., 2019, 2021; De Lombaerde et al., 2022). For example, climbing lizards regulate body temperature by their location in the canopy (Zlotnick et al., 2024). The current generation of big-leaf land surface models lacks sufficient detail of the within-canopy environment to study forest buffering. Hes et al. (2024), for example, used CLM5.1 to contrast the buffering capacity of forests and grasslands, but noted the model's inability to adequately resolve the canopy air space. The model's canopy parameterization reflects the heritage of land surface models as providing flux boundary conditions to the atmosphere (Manabe et al., 1965; Kasahara and Washington, 1967) rather than modeling the surface air. Observational analyses of forest influences on temperature likewise neglect air temperature within the canopy and instead focus on radiative land surface temperature or air temperature above the canopy (Li et al., 2025). The canopy physics of land surface models must be modernized for theoretical and computational advances and to enable study of forest microclimates.

Land surface models are routinely evaluated in comparison with observations of above-canopy fluxes obtained at eddy covariance flux towers, seen, for example, in the development of CLM (Stöckli et al., 2008; Burns et al., 2018) and as model benchmarking exercises (Best et al., 2015; Haughton et al., 2016; Abramowitz et al., 2024). If multilayer canopy models are to become a useful alternative to big-leaf models, comprehensive measurements of fluxes and scalar profiles within canopies are needed to identify model strengths and weaknesses and to advance theory and numerical parameterizations.

Here, we describe a dataset of flux and scalar measurements within and above a tree canopy and use the data to test a multilayer canopy model developed for CLM. Previous testing of the model demonstrated its performance in comparison with measurements of above-canopy fluxes and CLM5 (Bonan et al., 2018, 2021). For the current study, we use the high vertical resolution profile observations of air temperature, humidity, wind speed, and turbulent fluxes within and above the canopy of a walnut orchard obtained during the Canopy Horizontal Array Turbulence Study (CHATS; Patton et al., 2011). The CHATS campaign's design, instrument deployment strategy, horizontally homogeneous terrain and canopy, ample fetch, and range of wind speeds sampled provide a comprehensive dataset to evaluate fluxes and scalars simulated under a variety of stability regimes.

Our study targets evaluation of canopy processes in simulations forced with the observed meteorology above the canopy. We prepare a dataset of 30-min average statistics from 5-min average data and perform simulations for the May 2007 observational period. The dataset provides a benchmark with which to test multilayer canopy models. Our model–data comparison identifies the observations needed to test multilayer models, provides guidance to parameter estimation, highlights the potential of multilayer models to simulate the complex micrometeorology of forest canopies, and points to further research needs.

2. Methods

Simulation of the walnut orchard requires several steps: preparing the observations to evaluate the model; modifying the model to improve numerical methods; configuring the model for the walnut orchard; and running the model for the observational period, including sensitivity analyses to evaluate parameter choices.

2.1. Observations

2.1.1. CHATS field campaign

Turbulent exchange was measured within and above a walnut orchard (*Juglans regia* 'Chandler') located in Dixon, California during the Canopy Horizontal Array Turbulence Study (CHATS) from mid-March to mid-June 2007 (Patton et al., 2011). Measurements over the field campaign spanned the time before leaf emergence, the green-up transition, and after leaf emergence. The average canopy height was about 10 m. The cumulative plant area index was about 0.7 m^2 m^{-2} before leaf emergence, increasing to about 2.5 m^2 m^{-2} after leaf emergence. The soil is Yolo silty clay loam. Patton et al. (2011) describe the study. Several additional publications provide further information about CHATS (Dupont and Patton, 2012a,b; Shapkalijevski et al., 2016, 2017; Brown et al., 2020; Pan and Patton, 2017, 2020; Pan et al., 2025).

We use data from the 30-m tower, with 13 measurement levels located within the canopy, at the canopy top, and above the canopy (Table S.1). Winds and turbulent fluctuations were measured with sonic anemometers, and water vapor fluctuations were measured with krypton hygrometers. Incoming and outgoing shortwave and longwave radiation were measured at 16 m and 2 m. Precipitation was measured with a tipping bucket located in a clearing between rows of trees. Barometric pressure was measured at a height of 1 m on the tower. Soil moisture and soil heat flux were measured at 5 cm depth. For instrument model numbers and other deployment details, see Patton et al. (2011).

We focus on the month of May, when leaves were fully emerged, so as to include the effects of leaf physiology on turbulent fluxes. Figs. 1 and 2 show meteorological conditions for May. Conditions were generally clear sky, with incoming solar radiation above the canopy equal to 800–1000 W m^{-2} and few periods of rain. Soil moisture generally decreased over time (Fig. 2). Near the end of the month, the soil was irrigated at several times in a block pattern throughout the orchard.

2.1.2. Data processing

We use 5-min statistics generated from version 2 of the NSF National Center for Atmospheric Research (NSF NCAR) Earth Observing Laboratory (EOL) high-rate CHATS data (Horst and Oncley, 2019). Version 2 includes a sonic anemometer tilt-correction (Wilczak et al., 2001) and shadow-correction for the CSAT3 transducers (Horst et al., 2015). The tilt-correction was applied uniquely at every sonic level, and the EOL-determined planar-fit coefficients for each sonic anemometer are shown in Table S.1. More specific details about the CHATS instruments, EOL quality-control, and data processing can be found on the CHATS project webpage (2007). From the EOL 5-min means and covariances, we calculate 30-min statistics (including turbulent fluxes) following the procedures described in ISFS (2025). The 30-min data are centered in the averaging period (15 or 45 min past the hour) and times are Coordinated Universal Time UTC. Results are shown in CHATS local standard time (Pacific Standard Time; PST) which is 8 h behind UTC.

Corrections are applied to data collected by those instruments for increased accuracy. A brief summary of the corrections applied to calculate the turbulent fluxes is as follows: (1) The Schotanus correction is applied to correct the sensible heat flux for water vapor fluctuations (Schotanus et al., 1983; Foken et al., 2012), (2) water vapor

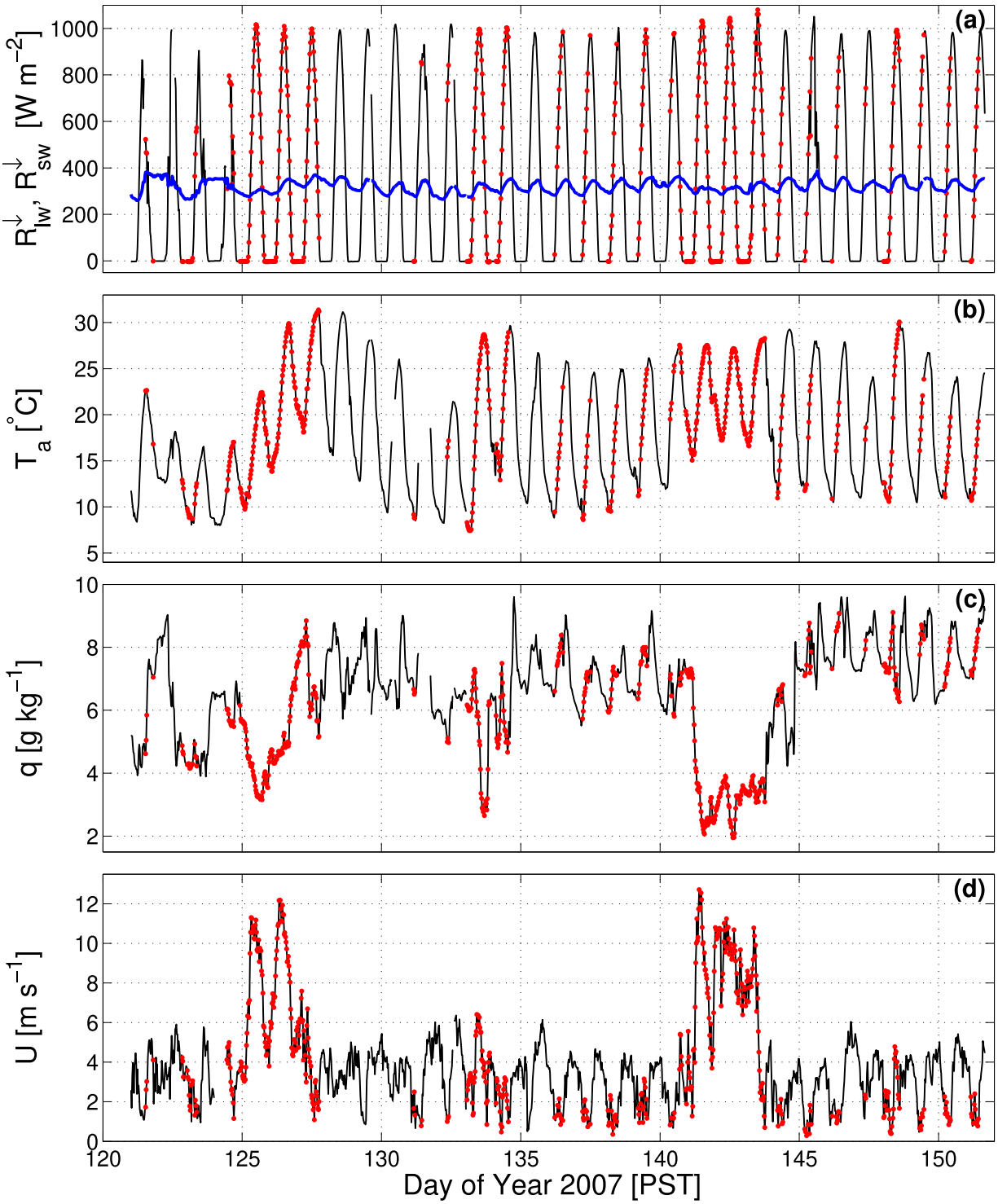

Fig. 1. Time series for May 2007 of observed 30-min mean above-canopy (a) 16-m incoming solar radiation ($R^{\downarrow}_{sw}$) and longwave radiation ($R^{\downarrow}_{lw}$; blue), (b) 23-m air temperature (T_a), (c) 23-m specific humidity (q), and (d) 23-m horizontal wind speed (U). The points shown in red are those eliminated due to footprint and wind direction considerations. In (a), the time periods shown in red also apply to $R^{\downarrow}_{lw}$. Data gaps are due to either precipitation, maintenance work being done to instruments on the tower, or instrument problems.

fluctuations measured using the krypton hygrometers are corrected for oxygen absorption following Oncley et al. (2007), and (3) The Webb–Pearman–Leuning correction is used to correct latent heat flux for sensible heat flux variations (Webb et al., 1980; Fuehrer and Friehe, 2002). The moist air density (ρ), specific heat (c_p), and latent heat of vaporization (λ) vary with air temperature, pressure, and humidity. Further details on the flux calculations and other data details are provided in Appendix A.

2.1.3. Data analysis

We screen the data to eliminate time periods during which the tower footprint was outside the boundary of the walnut orchard and also for

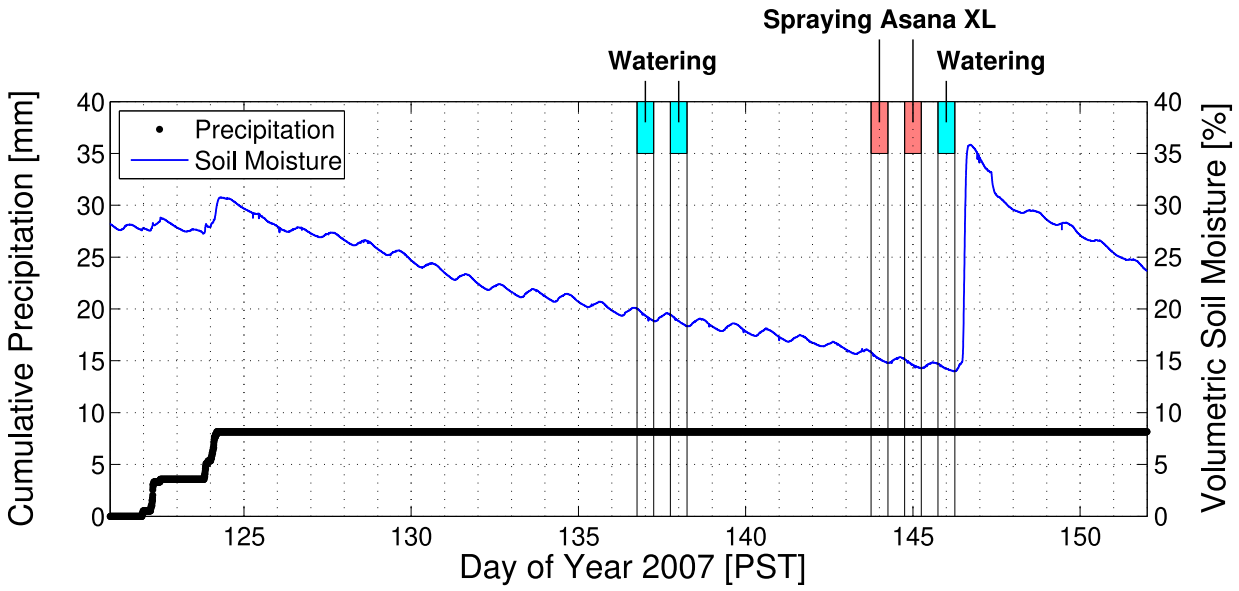

Fig. 2. Time series for May 2007 of observed cumulative precipitation and volumetric water content at 5-cm depth. Irrigation of the orchard is indicated by the text and light blue squares. The water was typically applied overnight (between 18:00 PST and 06:00 PST). Watering on the night of day 145 occurred near the instrumented tower, as noted by the sharp increase in soil moisture. The watering on the nights of days 136 and 137 occurred in other sections of the orchard. Spraying of the Dupont insecticide Asana XL on the nights of days 143 and 144 is highlighted by the red boxes.

strong advective conditions. We bin the remaining data into stability regimes based on the bulk Richardson number.

Footprint considerations. The 30-m tower was located about 130 m from the northern edge of the orchard to focus on winds from the south (Patton et al., 2011). We use 23-m measurements to examine footprint contours of the source area for 80% of the flux based on the footprint model from Kljun et al. (2015, https://footprint.kljun.net/). The analysis shows that winds from the north primarily sample outside the walnut orchard (Fig. S.1) while winds from the south sample the walnut orchard (Fig. S.2). Therefore, we exclude data when the above-canopy wind direction was from the north (0–90°, 270–360°). We use measurements at the 23-m height instead of 29-m to ensure that the orchard remains within the sensor's fetch during periods with stable stratification.

Figure S.3a provides a time series of above-canopy wind direction. At the orchard, the wind patterns are affected by the coastal mountain ranges to the west and Sierra Nevada mountains to the east, as well as sea-breezes that flow into the San Joaquin Valley, primarily through San Francisco Bay following the Sacramento River (Zaremba and Carroll, 1999; Mayor, 2011, 2017). For the May observations, high-wind periods (i.e., $U > 10$ m s^{-1}) were exclusively from the north (Fig. S.3b). The wind direction also had a strong time-of-day dependence. Winds for a typical four-day period in May were often from the north early in the morning (Fig. S.4). For the entire month of May, about 70% of the 30-min periods between 08:00–10:00 PST were north winds while only 20%–30% of the afternoon and evening periods were north winds (Fig. S.3c). Therefore, the flux footprint restriction removes all high wind periods and most of the early morning periods (i.e., those shown in red in Fig. 1) from our analysis.

Stability considerations. We stratify the remaining data by the above-canopy bulk Richardson number (Ri_b) to compare the model with observations for particular stability regimes. We calculate Ri_b from the 30-min observations using:

$$Ri_b = \frac{g}{\overline{\theta}} \frac{(\theta_U - \theta_L)(z_U - z_L)}{(U_U - U_L)^2} \quad (1)$$

where z_U and z_L are the 23-m and 10-m measurement heights, respectively, θ_U and θ_L are the potential air temperature at the measurement level, $\overline{\theta}$ is the average of θ_U and θ_L, U_U and U_L are the horizontal scalar mean wind speed, and g is gravitational acceleration. For our analysis, we bin the observations and model output into five broad stability regimes based on the observed Ri_b: strongly unstable (SU; $-10 \le Ri_b \le -0.1$), weakly unstable (WU; $-0.1 \le Ri_b \le -0.01$), near-neutral (NN; $-0.01 \le Ri_b \le 0.01$), weakly stable (WS; $0.01 \le Ri_b \le 0.2$), and strongly stable (SS; $0.2 \le Ri_b \le 100$). We use the observed Ri_b to bin both the observations and the model so that the measurements and the model output correspond in time.

The bin boundaries are based on apparent changes in the observations. There is a well-known transition from weakly stable to strongly stable conditions at around $Ri_b \approx 0.2$ (Businger, 1973; Galperin et al., 2007; Burns et al., 2011). Previous work with CHATS data used h/L, where h is the canopy height and L is the Obukhov length, as the stability parameter (Dupont and Patton, 2012a,b). Both h/L and Ri_b change with stability, and relationships between them have been considered in many past studies (Businger et al., 1971; Mauritsen and Svensson, 2007; Burns et al., 2011).

Advection. Examination of the observed fluxes in relation to Ri_b reveal counter-intuitive fluxes for a small number of 30-min time intervals that are highlighted by the colored circles in Fig. S.5. First, there are stable periods ($Ri_b > 0$) with positive net radiation ($R_{net} > 0$), which in combination suggests non-stationary or advective conditions. Stable periods are usually nighttime phenomenon, but these few periods occur in the late afternoon. They coincide with the arrival of the density current fronts documented by Mayor (2011). Therefore we exclude these data points (34 samples) from our analysis, though they do not significantly impact our model-observation comparison.

The other counter-intuitive fluxes highlighted in Fig. S.5 are unstable data with negative net radiation ($Ri_b < 0$ and $R_{net} < 0$). These data periods occur later in the evening than the sea-breeze frontal passages. They are periods with wind speed on the order of 4–6 m s^{-1} and the temperature gradient is small. These periods are similar to the near-neutral points with $Ri_b > 0$ and because the near-neutral category includes both unstable and stable points, we include these data in our analysis.

2.2. The multilayer canopy model

2.2.1. Model description

CLM-ml is a multilayer canopy model parameterizing the relationship between state variables and fluxes designed for inclusion in the Community Land Model (Bonan et al., 2018, 2021). The canopy model uses an implicit solution to solve the flux–profile calculations as a system of linear equations. One-dimensional (vertical) continuity equations for potential temperature and water vapor concentration (equal to vapor pressure divided by surface pressure) are combined with equations for leaf and soil energy balances and are solved as an implicit system of tridiagonal equations for potential temperature, water vapor concentration, and leaf temperatures (sunlit and shaded leaves) at each layer in the canopy, as well as ground temperature. The scalar continuity equations balance the vertical flux divergence and storage in the canopy air space with leaf source/sink fluxes and ground fluxes. The model uses a first-order turbulence closure combined with the Harman and Finnigan (2007, 2008) roughness sublayer parameterization to calculate wind speeds and scalar diffusivities within and above the canopy. Leaf fluxes of sensible and latent heat are calculated from the leaf energy balance (including a heat storage term) for sunlit and shaded leaves at each canopy layer. Leaf gas exchange is calculated using principles of water-use efficiency optimization and plant hydraulics. Optimization is attained when further stomatal opening does not yield sufficient carbon gain per unit water loss (defined by a marginal water-use efficiency parameter) and with the constraint that stomata close as leaf water potential decreases. Leaf nitrogen (per unit leaf area) decreases from the top to the bottom of the canopy, resulting in a decrease in photosynthetic capacity at lower levels in the canopy. Bonan et al. (2014) provide the equations for leaf gas exchange, stomatal conductance, and plant hydraulics, Bonan et al. (2018) give the roughness sublayer parameterization and the flux–profile solution, and Bonan et al. (2021) describe the generalization of the model to any number of canopy layers. The model has been tested against above-canopy flux data at several AmeriFlux sites (Bonan et al., 2018, 2021).

For the CHATS simulations, we modify the model source code from CLM-ml v1 (Bonan et al., 2021) and denote the revised model CLM-ml v2. An overarching goal is to reduce, or at least provide rationale for, numerical constraints used in the canopy flux parameterization so that they are implemented in a less arbitrary manner (Table 1). We contrast the numerical methods in CLM-ml with those used in version 5 of the Community Land Model (CLM5) and the forthcoming version 6 (CLM6) to highlight key approximations and constraints in the models. The changes between CLM-ml v1 and CLM-ml v2 are:

State updates. A numerical challenge in calculating canopy fluxes is that the fluxes depend on state variables, but the state variables depend on fluxes. More formally, the time change in state variable y depends on y at time t (i.e., $dy/dt = f'(t, y)$). For example, net radiation and stomatal conductance, which are needed to calculate leaf fluxes, depend on leaf temperature, which itself changes over a model timestep. Stomatal conductance likewise depends on leaf water potential, which depends on transpiration. A key timestepping dependency occurs among the Obukhov length, sensible heat flux, and latent heat flux. Additional dependencies are: the wetted fraction of the canopy depends on evaporation, but evaporation depends on the wetted fraction; and leaf boundary layer conductance varies with wind speed.

CLM5 resolves these interdependencies using an iterative solution to simultaneously solve the equation set over a timestep $\Delta t = 30$ min (Lawrence et al., 2018). A maximum of 40 iterations is allowed, but convergence is not guaranteed. Ad-hoc corrections that set atmospheric stability to near-neutral conditions if it switches between stable and unstable values during the iteration, repartition energy between latent and sensible heat, and limit the change in vegetation temperature to <1 K are encoded in the numerical solution (Table 1). CLM6 retains the 40 iteration maximum in its standard configuration and has a fast configuration with 3 iterations.

CLM-ml v1 uses the Euler method to advance the canopy state from time n to $n+1$ with $\Delta t = 5$ min (i.e., $y_{n+1} = y_n + \Delta y$). The 5-min step size lessens the temporal mismatch between state variables and fluxes. CLM-ml v2 replaces the Eulerian solution with a fourth-order Runge–Kutta method. Runge–Kutta methods provide a robust numerical solution to a differential equation in which Δy depends on y. The equation set is solved for Δy using four Runge–Kutta substeps: (1) y_0 from the previous timestep is used to obtain Δy_1; (2) $y_0 + 0.5\Delta y_1$ is used to obtain Δy_2; (3) $y_0 + 0.5\Delta y_2$ is used to obtain Δy_3; and (4) $y_0 + \Delta y_3$ is used to obtain Δy_4. The weighted average of the four Runge–Kutta substeps, $y_0 + (\Delta y_1 + 2\Delta y_2 + 2\Delta y_3 + \Delta y_4)/6$, is used in a 5th call to the flux–profile equation set in the final solution. State variables updated this way are air temperature, vapor pressure, leaf temperature (sunlit and shaded), leaf water potential (sunlit and shaded), intercepted water, and ground temperature.

Meteorological forcing. CLM5/6 uses a 30-min timestep for coupling with its host atmosphere model as part of the Community Earth System Model (Danabasoglu et al., 2020). When running CLM5/6 at tower sites uncoupled from the atmosphere model, tower meteorology replaces the atmospheric model. CLM-ml v1 retains CLM5/6's 30-min timestep. The atmospheric forcing is provided at 30-min resolution and is held constant over the six 5-min steps. Model output is averaged over the six 5-min steps and reported as 30-min values.

CLM-ml v2 interpolates the 30-min forcing data to the 5-min steps. The interpolation is linear over the six 5-min steps using values at the previous, current, and next 30-min timesteps. For the CHATS data, the 30-min forcing is centered in the time interval (i.e., 15 min or 45 min), and the 5-min interpolation is likewise centered in its time interval (e.g., 2.5, 7.5, 12.5, 17.5, 22.5, 27.5 min). Precipitation is not interpolated. A three-point interpolation is possible because the meteorological data is available for the full time series. In coupling to the host atmospheric model, where forcing values are known backwards in time but not forward, the interpolation could only use the current and previous values of the 30-min forcing variable.

CLM5 restricts the forcing height wind speed to >1 m s^{-1} to prevent sensible and latent heat fluxes from being small with calm conditions (Lawrence et al., 2018), and CLM6 retains this restriction. CLM-ml v1 likewise uses the same restriction. In CLM-ml v2, we lower the minimum wind speed threshold to 0.5 m s^{-1}, which is representative of calm air on the Beaufort scale, without a degradation in model performance.

Universal similarity functions. CLM-ml v1 uses the universal functions ϕ_m and ϕ_c and the roughness sublayer modified functions $\hat{\phi}_m$ and $\hat{\phi}_c$ from Harman and Finnigan (2007, 2008) (see Bonan et al., 2018, their Eqs. A10, A11, A14, A18). These are used to obtain the associated ψ_m and ψ_c functions and the roughness sublayer modified functions $\hat{\psi}_m$ and $\hat{\psi}_c$ (see Bonan et al., 2018, their Eqs. A12, A13, A17). The $\hat{\psi}$ functions are evaluated numerically, with values obtained from a lookup table (see Bonan et al., 2018, their Eq. A21). For CLM-ml v2, we reevaluate the lookup table from that used in Bonan et al. (2018, 2021) for more numerical precision.

ϕ_m and ϕ_c become increasingly large with more strongly stable conditions, which produces excessively cold canopy temperatures at night. CLM-ml v1 restricts the value of the Obukhov length (L) used in the similarity functions under strongly stable conditions. The restriction is imposed as $\zeta = (z - d)/L \leq 1$ on the stable side, where z is the atmosphere forcing height and d is the displacement height. At the walnut orchard, with $z = 23$ m and $d \approx 8$ m, this means that $L \geq 15$ m. The ζ restriction originates with CLM5, which imposes $\zeta \leq 0.5$ in the stable regime; CLM6 increases the limit to $\zeta \leq 2$ when biomass heat storage is enabled. In CLM-ml v2, we revise the constraint on L based on applicability of the roughness sublayer theory across a range of stability regimes.

Table 1
Constraints imposed on canopy flux calculations in CLM5, CLM6, CLM-ml v1, and CLM-ml v2. Notation: Δt, timestep; z, atmospheric forcing height; d, displacement height; L, Obukhov length; u_{ref}, forcing height wind speed; L_c, canopy length scale; u_*, friction velocity; $U(h)$, wind speed at canopy height; U_{af}, CLM canopy wind speed; U_i, wind speed at each layer in the canopy; ρ_m, molar density; $g_{bh,i}$, leaf boundary layer conductance for heat at each layer in the canopy; $g_{a,i}$, aerodynamic conductance at each layer in the canopy. The minimum restriction to u_{ref}, maximum cap to ζ under stable conditions, and maximum iterations in CLM6 are user-specified parameters. Shown are supported model configurations. N/A denotes the constraint is not relevant to the particular model, and – means the constraint is not imposed.

Constraint	CLM5	CLM6	CLM-ml v1	CLM-ml v2
Timestep	$\Delta t = 30$ min	As in CLM5	$\Delta t = 5$ min	$\Delta t = 5$ min
Numerical methods for canopy solver	Iterative: 40 maximum	As in CLM5 with 40 (standard) or 3 (fast)	Euler	Runge–Kutta methods (4th-order)
Atmospheric stability $\zeta = (z-d)/L$	If ζ changes sign four or more times during the iteration, set $\zeta = -0.01$	As in CLM5	–	–
Latent heat flux (λE)	If λE changes sign from the previous iteration, λE is constrained to 10% of the computed value and the difference is added to sensible heat (H)	As in CLM5	–	–
Latent heat flux (λE)	If canopy evaporation exceeds the intercepted water, the energy error is added to H	As in CLM5	–	–
Vegetation temperature	The change in vegetation temperature is constrained to <1 K during an iteration and the energy error is added to H	As in CLM5	–	–
Meteorological forcing	30-min	As in CLM5	30-min	30-min interpolated to 5-min
Forcing height wind	$u_{\mathrm{ref}} \geq 1$ m s^{-1}	As in CLM5	$u_{\mathrm{ref}} \geq 1$ m s^{-1}	$u_{\mathrm{ref}} \geq 0.5$ m s^{-1}
Obukhov length (L)	L constrained with $\zeta \leq 0.5$	As in CLM5 with $\zeta \leq 2$	As in CLM5 with $-2 \leq \zeta \leq 1$	$-2 \leq L_c/L \leq 1$
$\beta = u_*/U(h)$	N/A	N/A	$0.2 \leq \beta \leq 0.5$	–
Canopy wind speed, leaf boundary layer conductance	$U_{af} = u_*$	As in CLM5	$U_i \geq 0.1$ m s^{-1}	$\rho_m/g_{bh,i} \leq 211$ s m^{-1}
Aerodynamic conductance	–	–	$\rho_m/g_{a,i} \leq 500$ s m^{-1}	$\rho_m/g_{a,i} \leq 500$ s m^{-1}

Applicability of roughness sublayer theory. For stable conditions, the roughness sublayer theory is applicable for $L_c/L \leq 2.2\kappa/(\gamma\beta)$, where $L_c = (c_d\, a)^{-1}$ is the canopy adjustment length scale (m) with canopy-element-level drag coefficient c_d and frontal plant area density a, $\kappa = 0.4$ is the von Kármán constant, and $\beta = u_*/U(h)$ is the ratio of friction velocity to mean horizontal wind speed at the canopy top (see Harman and Finnigan, 2007, their Eq. 25). γ is the turbulent Prandtl number at canopy top and has a value in the range 0.5–1. The Harman and Finnigan (2007) constraint means that $L_c/L \leq 2.5-5.0$ in weakly stable regimes (in which $\beta = 0.35$ is representative) and $L_c/L \leq 3.5-7.0$ in strongly stable regimes (with $\beta = 0.25$). Harman and Finnigan (2008) simplified the constraint to $-2 \leq L_c/L \leq 2$, including unstable regimes, and Harman (2012) noted that $-1 \leq L_c/L \leq 1$ is appropriate for the Tumbarumba OzFlux site, a tall eucalyptus forest.

At the walnut orchard, $L_c = 14.8$ m with the leaves emerged. The constraint $L_c/L \leq 2$ means that $L \geq 7.4$ m on the stable side, which allows for more stable conditions that in CLM-ml v1. $L_c/L \leq 1$ gives $L \geq 14.8$ m, which is similar to the restriction imposed in CLM-ml v1. Given uncertainty in the limits to the roughness sublayer theory on the stable side, we impose the restriction $-2 \leq L_c/L \leq 1$ in CLM-ml v2. The observations show that L_c/L rarely reaches a value of 2, and the bulk of the measurements are between –1 and 1 (Fig. 3).

Harman (2012) parameterization of β. Calculating β is a key component of the Harman and Finnigan (2007, 2008) roughness sublayer parameterization (see Bonan et al., 2018, their Eqs. A22–A24). β depends on L_c/L and can attain excessively large values with strongly unstable conditions (large negative values of L_c/L). Harman (2012) revised the parameterization so that β does not increase indefinitely with increasing unstable conditions (see his Eq. 13). The modification recognizes that β deviates from the Harman and Finnigan (2007, 2008) roughness sublayer value with increasingly unstable conditions and instead is closer to the value attained when neglecting roughness sublayer influences. The revised parameterization is:

$$\beta = \begin{cases} \beta_{\mathrm{HF}} & \text{for } L_c/L > a_2 \\ \beta_{\mathrm{norsl}} + \frac{\beta_{\mathrm{HF}} - \beta_{\mathrm{norsl}}}{1 + a_1 |L_c/L - a_2|^{a_3}} & \text{for } L_c/L \leq a_2 \end{cases} \tag{2}$$

β_{HF} is the roughness sublayer value as in Harman and Finnigan (2007, 2008), obtained from $\beta_{\mathrm{HF}}\, \phi_m \left(\beta_{\mathrm{HF}}^2\, L_c/L\right) = \beta_{\mathrm{N}}$ with β_{N} the value for β in neutral stability conditions. β_{norsl} is the value without the roughness sublayer influence, obtained from $\beta_{\mathrm{norsl}}\, \phi_m(\beta_{\mathrm{norsl}}^2\, L_c/L) = \kappa/2$.

β_{N}, a_1, a_2, and a_3 are canopy specific parameters. Harman (2012) estimated a_1–a_3 by fitting Eq. (2) to 30-min observations at Tumbarumba. He noted that β shows considerable scatter and grouped the data into 12 composite bins to obtain $a_1 = 2$, $a_2 = -0.15$, and $a_3 = 1.5$ with $\beta_{\mathrm{N}} = 0.374$. Using $\beta_{\mathrm{N}} = 0.35$ (from Bonan et al., 2018, 2021) and fitting Eq. (2) to the CHATS data by minimizing the sum of square difference with the observations yields $a_1 = 0.89$, $a_2 = -0.07$, and $a_3 = 2.19$ (Fig. 3). Eq. (2) eliminates the need for the upper limit to β used in CLM-ml v1.

Canopy wind and leaf boundary layer conductance. CLM5 approximates the wind speed in the canopy as $U_{af} = u_*$ when calculating the leaf boundary layer conductance (see Lawrence et al., 2018, their Eq. 2.5.117), and CLM6 retains this approximation. CLM-ml v1 assumes an exponential in-canopy wind profile to calculate wind speed at each level in the canopy, but enforces a minimum wind speed of 0.1 m s^{-1} so that the leaf boundary layer conductance does not attain small values.

For CLM-ml v2, we remove the minimum wind speed restriction and instead impose a minimum leaf boundary layer conductance for heat equal to 0.2 mol m^{-2} s^{-1}. (CLM-ml uses conductance with molar units. The minimum conductance is equivalent to a resistance of 211 s m^{-1} at standard temperature and pressure with molar density $\rho_m = 42.3$ mol m^{-3}.) The chosen minimum conductance is that for a large leaf (10 cm) exposed to calm winds (0.1 m s^{-1}). CLM5 uses a leaf dimension of 4 cm (Lawrence et al., 2018), and we use the same value for walnut. For a 4-cm leaf, the minimum conductance of 0.2 mol m^{-2} s^{-1} is attained at

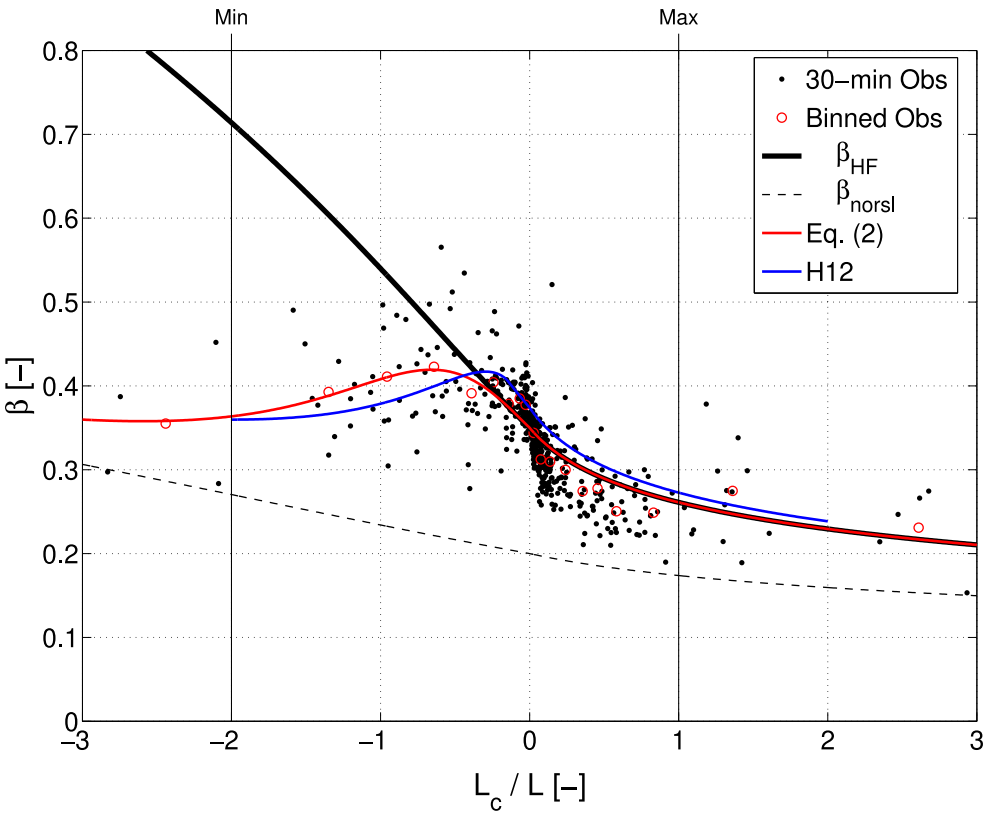

Fig. 3. β plotted in relation to L_c/L. Both variables are dimensionless (denoted by –). Observations are shown as 30-min values (closed black circles) and as binned averages (open red circles). The solid black line shows the Harman and Finnigan (2007, 2008) functional relationship (β_{HF}), and the dashed line shows β calculated without the roughness sublayer (β_{norsl}) as in Harman (2012). The red line shows the revised (Harman, 2012) parameterization, given by Eq. (2), fitted to the binned data. For comparison, the functional form given by Harman (2012) for Tumbarumba is shown as a blue line (H12; $\beta_N = 0.374$ and the data span $|L_c/L| < 2$). Note that β_{HF} and Eq. (2) are identical for $|L_c/L| > -0.07$. The vertical black lines highlight the constraint $-2 \le L_c/L \le 1$ used in the model.

a wind speed equal to 0.04 m s^{-1}. The boundary layer conductances for water vapor and CO_2 are obtained from that for heat after adjusting for the diffusivity of H_2O and CO_2 (see Bonan et al., 2014, their Eq. A9).

Aerodynamic conductance. CLM-ml v1 uses the Harman and Finnigan (2007, 2008) parameterization of eddy diffusivity to calculate aerodynamic conductances in the canopy (see Bonan et al., 2018, their Eqs. 25, 26). The parameterization extends to the ground surface as described by Bonan et al. (2021). CLM-ml v2 replaces the diffusivity in the first layer immediately above the ground with an aerodynamic conductance calculated using the log-law profile (see Bonan et al., 2018, their Eq. 27). With layer thickness $\Delta z = 50$ cm as in previous simulations (Bonan et al., 2018, 2021), the conductance extends from the height of the lowest canopy layer ($z_1 = 25$ cm) to the ground roughness length.

Constraints are placed so that the aerodynamic resistance (the inverse of conductance) within a layer (i.e., integrated over the layer thickness $\Delta z = 50$ cm) does not exceed 500 s m^{-1}. This value is arbitrary, but accommodates extremely small conductances (large resistances) within the canopy under strongly stable conditions and is needed to prevent numerical instability in the flux–profile solution when turbulent mixing is low.

Stomatal conductance. CLM-ml v2 uses bisection to numerically solve for the stomatal conductance that maximizes water-use efficiency. Bisection ensures the algorithm converges on a root while the numerical solver used in CLM-ml v1 does not.

2.2.2. Site parameters

For the current simulations, the multilayer canopy model is configured with parameters specific to the walnut orchard. These are:

Soil texture. The model uses the same soil thermal and hydraulic parameters as CLM5. Soil texture is silty clay loam (10% sand, 34% clay). The soil organic matter content is 38%, which adjusts soil thermal and hydraulic parameters from their mineral soil values. The time series of soil thermal conductivity compares favorably with the observations, though the model thermal conductivity is biased low in early- and late-May, when the soil is wet (Fig. S.6). The depth to bedrock in the model is set to 2 m, which is the active soil column for hydrology.

Soil color. Soil color classes range from 1 (light) to 20 (dark) as in CLM5. We set the soil color class to 15. This value is obtained by comparing the model's simulated albedo with the observed albedo. It minimizes the bias between the albedo simulated with the model's radiative transfer and the observed albedo at the 2-m measurement height averaged over the leafless period 1–8 April (Fig. S.7). The above-canopy albedo is less sensitive to soil color than is the 2-m albedo. For comparison, the forest sites simulated in Bonan et al. (2018, 2021) have soil color ranging from 15 to 20.

Plant area density. Canopy height during CHATS was $h = 10$ m. Plant area density profiles were collected sporadically during CHATS, and time-averages of those observations were reported individually for the leafless and full-leaf periods (Patton et al., 2011). However, the model requires a continuous time-series of both stem area and leaf area density. To obtain these time-series, we first assume that the vertical profile of plant area density (m^2 m^{-3}) can be specified using a beta distribution in which:

$$a(z) = \frac{P}{h} \frac{(z/h)^{p-1}\,(1 - z/h)^{q-1}}{B(p,q)}, \tag{3}$$

where P is the canopy plant area index (i.e., the vertically-integrated frontal plant area density; m^2 m^{-2}), h is canopy height (m), z is

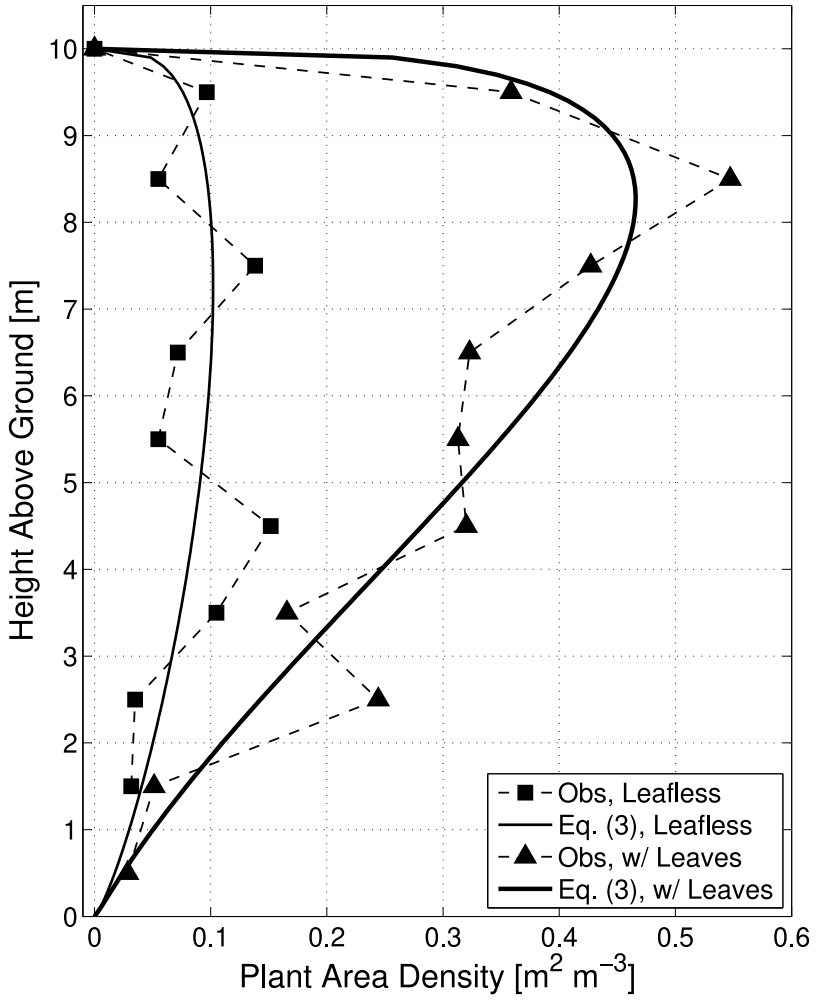

Fig. 4. Observed and modeled plant area density without leaves (leafless) and with leaves (w/ leaves). In Eq. (3), $p = 1.8$ and $q = 1.3$ for stems ($R^2 = 0.535$), and $p = 2.6$ and $q = 1.3$ ($R^2 = 0.782$) for leaves. The leafless observations show stem area, and the with-leaves observations show the combined stem and leaf area. The stem area index of the canopy is 0.74 m^2 m^{-2} and the leaf area index is 2.04 m^2 m^{-2}.

height (m), B is the beta function, and p and q are parameters (Bonan et al., 2018). To obtain profiles of stem area density, total plant area density measurements during the leafless period are fit using Eq. (3) to obtain p and q (Fig. 4). Leaf area density is estimated from the total plant area density measurements collected during the leaf-on period and subtracting the stem area. The beta function forces a to zero at the ground. An alternative function used by Massman et al. (2017) and Hung et al. (2024) allows for more foliage distribution shapes.

Stem area index is assumed to be constant (0.7 m^2 m^{-2}). The timing of the leaf area progression from no-leaves to fully-leafed is estimated from photographs taken during the field campaign. In the model, leaf area index is zero before 9 April, ramps up to 2.0 m^2 m^{-2} during the period between 10 April–1 May (linear interpolation), and thereafter remains constant. Fig. 5a shows the time series of plant area density.

Canopy element drag coefficient. In previous simulations, the drag coefficient for canopy elements is $c_d = 0.25$ (Harman and Finnigan, 2007, 2008; Bonan et al., 2018, 2021). To target CHATS, we calculate local canopy drag coefficients at each height where within-canopy observations are available according to Brunet et al. (1994), i.e.:

$$C_D(z) = -\frac{\partial \overline{u'w'}/\partial z}{a U^2}, \tag{4}$$

where a is the plant area density from Eq. (3). Central-differences are used to calculate the vertical gradient of $\overline{u'w'}$. Note that C_D is a local drag coefficient (which varies with height z), but the model requires a single aerodynamic drag coefficient (c_d). Figure S.8 shows the time series of C_D within the canopy. C_D at the three lowest levels (1.5, 3, and 4.5 m) has large temporal variability arising from variability in $\partial(\overline{u'w'})/\partial z$ whereas U^2 changes only a little. In contrast, C_D is smoother at the uppermost three levels (6, 7.5, and 9 m). Because the Harman and Finnigan (2007, 2008) roughness sublayer theory is most applicable in the upper canopy, we estimate c_d by averaging C_D over the uppermost three measurement levels. (Note that this c_d differs from the integral drag coefficient discussed in Mahrt et al. (2000); see Finnigan et al. (2015) for additional discussion.)

Fig. 5b shows the time series of c_d. The values are relatively constant during May, and the average for the month is 0.23. This is sufficiently close to the value used in Harman and Finnigan (2007, 2008) and Bonan et al. (2018, 2021); therefore we retain $c_d = 0.25$. The Harman and Finnigan (2007, 2008) theory relies on the inseperable combination of c_d and a through the canopy length scale $L_c = (c_d\, a)^{-1}$ rather than relying solely on c_d. Fig. 5c shows the time series of L_c. The average for May is $L_c = 14.8$ m.

2.2.3. Walnut physiology parameters

We use plant physiology parameters for a broadleaf deciduous temperate tree as in Bonan et al. (2014, their Table 3), Bonan et al. (2018, their Table 1), and Bonan et al. (2021, their supplemental Eq. 14), except as shown in Table 2 and obtained specifically for walnut from a survey of the literature. These parameters are described as follows:

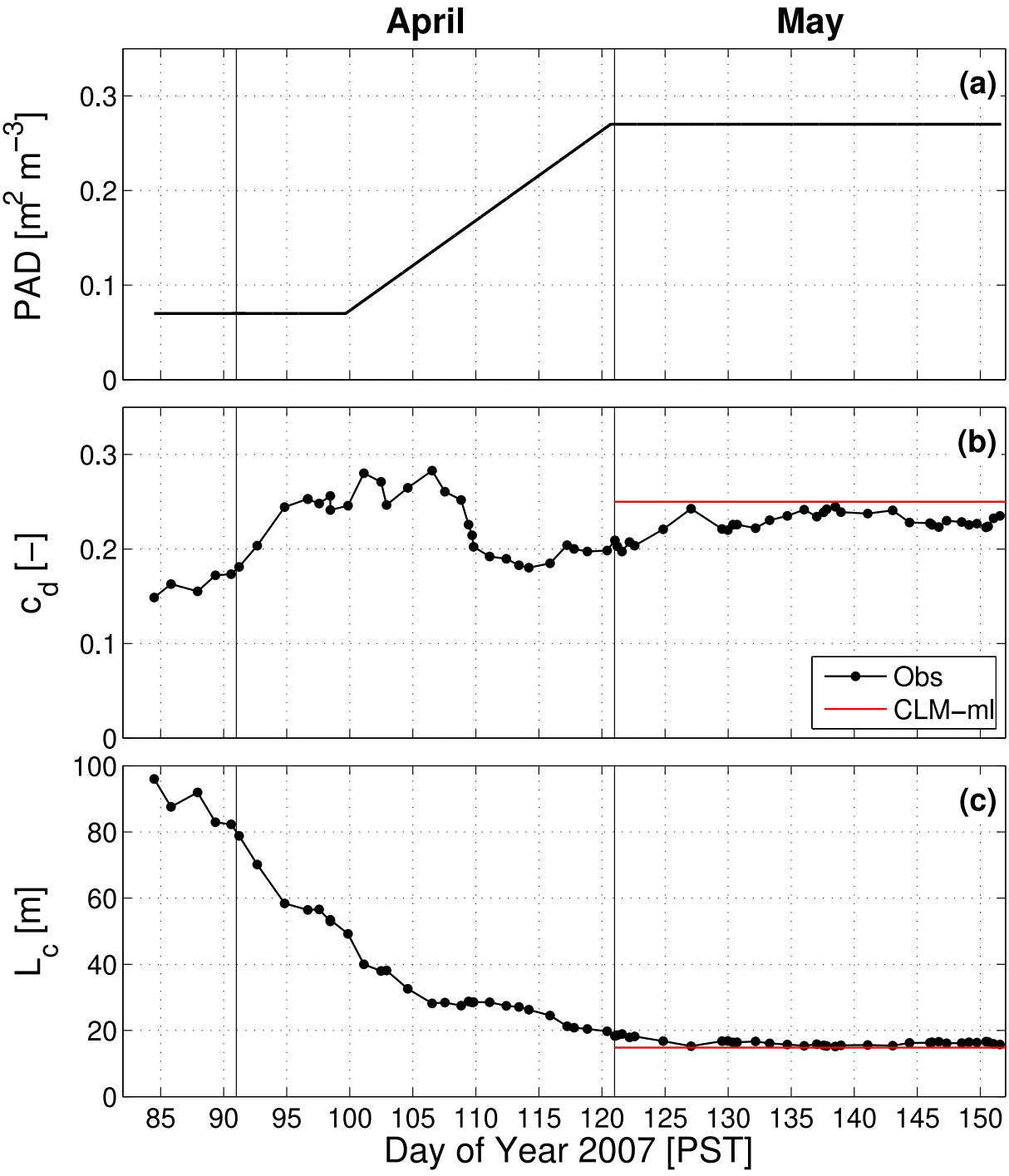

Fig. 5. Time series from late March to the end of May 2007 of (a) canopy plant area density (PAD) used in CLM-ml, (b) drag coefficient (c_d; dimensionless denoted by –), and (c) canopy length scale (L_c). The vertical lines denote transitions between months. PAD is the canopy plant area index (P) divided by canopy height (h). c_d is calculated based on data between 09:00–16:00 PST and within a 7-day sliding window moved one day at a time. Time periods with wind from the north are excluded, as discussed previously. c_d is plotted in relation to the mean of the time periods used in the 7-day sliding window and therefore is not evenly spaced because of missing data. L_c is calculated from PAD and c_d. The red line in (b) and (c) shows the average of the observations for May.

Leaf gas exchange. We estimate parameters governing leaf photosynthesis (A_n) and stomatal conductance (g_s) specific for *Juglans regia*. The parameter V_{cmax25}, which is the maximum rate of carboxylation at 25 °C, sets the maximum A_n at light saturation. The parameter ι is the marginal water-use efficiency and determines g_s for a given A_n. Bonan et al. (2014) showed that V_{cmax25} and ι can be estimated from leaf gas exchange measurements of A_n and g_s. Rosati et al. (2006) measured A_n and g_s for non-water stressed light saturated leaves at a 10-year-old *Juglans regia* 'Chandler' orchard in central California. The observations show maximum A_n equal to 25–27 μmol CO_2 m^{-2} s^{-1} and g_s as high as 0.8–0.9 mol H_2O m^{-2} s^{-1} (see their Fig. 2). V_{cmax25} = 125 μmol m^{-2} s^{-1} and ι = 375 μmol CO_2 mol^{-1} H_2O (Table 2) replicate the maximum

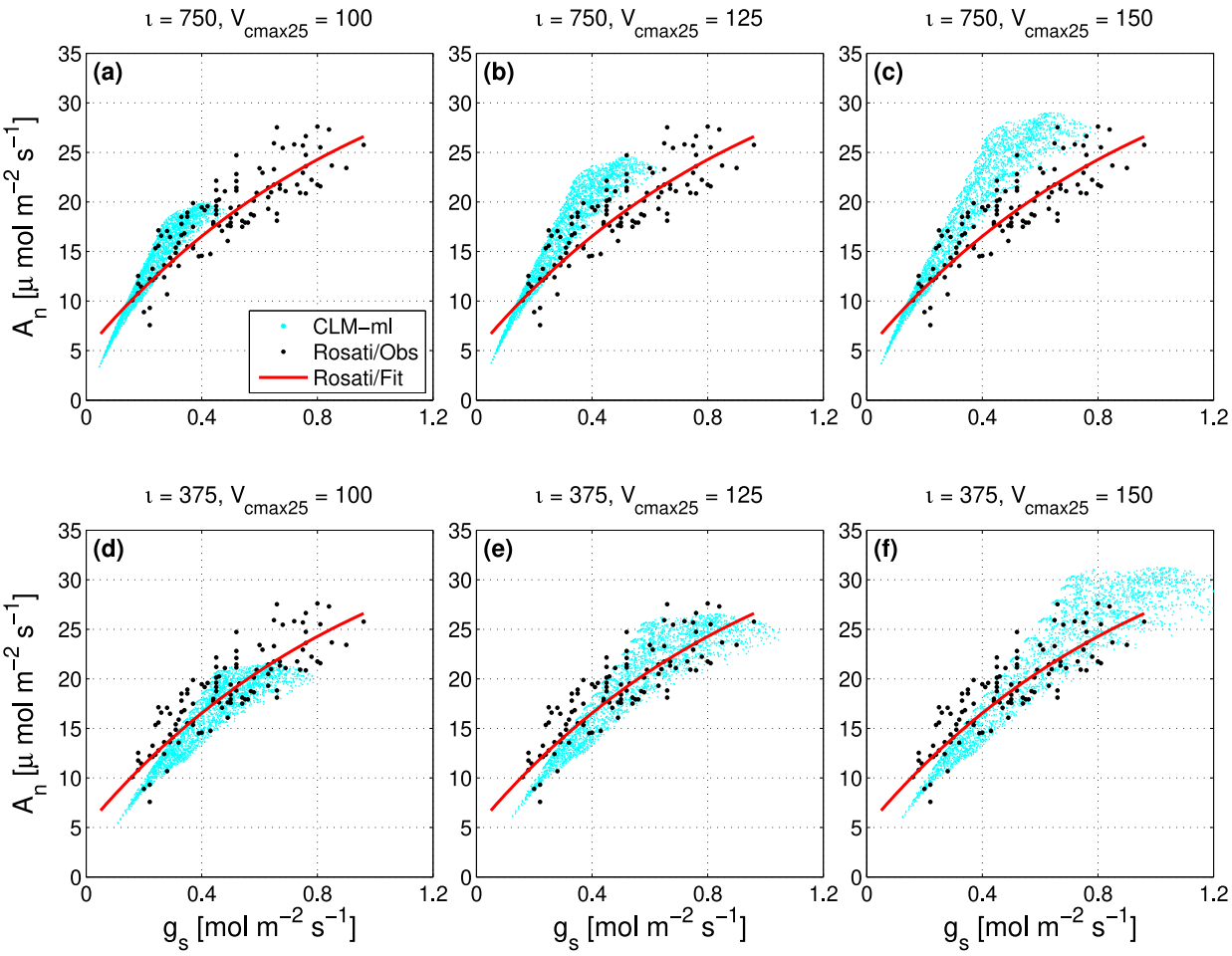

Fig. 6. Modeled and observed relationship between stomatal conductance (g_s; mol H_2O m^{-2} s^{-1}) and photosynthesis (A_n; μmol CO_2 m^{-2} s^{-1}). Modeled data (light blue symbols) are from CLM-ml for non-water stressed sunlit leaves at light saturation (absorbed photosynthetically active radiation ≥1200 μmol m^{-2} s^{-1}) over the month of May 2007. Shown are results using ι = 750 (a–c) and 375 (d–f) μmol CO_2 mol^{-1} H_2O and for V_{cmax25} = 100 (a,d), 125 (b,e), and 150 (c,f) μmol m^{-2} s^{-1}. For clarity, only every 5th data point is plotted. Also shown are the Rosati et al. (2006) observations for non-water stressed light saturated leaves (black symbols; see their Fig. 2). Only observations for g_s greater than approximately 0.2 mol H_2O m^{-2} s^{-1} are shown, for clarity. The red line is the regression fit reported by Rosati et al. (2006).

Table 2
Parameters modified in the multilayer canopy model specific for CHATS. Shown are the default values in CLM-ml v1 (Bonan et al., 2021) and the values used in the CHATS simulations. Reflectance (ρ) and transmittance (τ) for leaf and stem are given for the visible and near-infrared wavebands.

Category	Symbol	Description	Units	CLM-ml v1	CHATS
Leaf gas exchange	V_{cmax25}	Maximum carboxylation rate at 25 °C	μmol m^{-2} s^{-1}	57.7	125
	ι	Marginal water-use efficiency	μmol CO_2 mol^{-1} H_2O	750	375
Leaf water relations	ψ_{50}	Leaf water potential at 50% conductance	MPa	−2.3	−1.6
	α	Shape parameter for stomatal closure	–	40	40
Plant hydraulics	k_p	Hydraulic conductance of stems	mmol H_2O m^{-2} [leaf area] s^{-1} MPa^{-1}	4	7
	R_r^*	Fine root hydraulic resistivity	MPa s g $mmol^{-1}$ H_2O	25	14
Vegetation optics	ρ_{leaf}	Leaf reflectance (VIS, NIR)	–	0.10, 0.45	0.06, 0.42
	τ_{leaf}	Leaf transmittance (VIS, NIR)	–	0.05, 0.25	0.04, 0.43
	ρ_{stem}	Stem reflectance (VIS, NIR)	–	0.16, 0.39	0.21, 0.49
	χ_l	Leaf angle departure from spherical	–	0.25	0.53

rates, as well as the overall relationship between A_n and g_s (Fig. 6e). ι = 750 μmol mol^{-1} produces too steep of a relationship between A_n and g_s compared with the observations (Fig. 6a–c). V_{cmax25} = 100 μmol m^{-2} s^{-1} gives too low maximum A_n and g_s compared with the observations (Fig. 6a,d), and a value of 150 μmol m^{-2} s^{-1} produces high biases in maximum A_n (Fig. 6c,f).

Leaf water relations. In CLM-ml v0, stomata remain open until leaf water potential (ψ_l) reaches some minimum value ($\psi_{l,min}$ = −2 MPa), below which stomata are closed (Bonan et al., 2018). This is the same as the SPA model (Williams et al., 1996), from which the plant hydraulics modeling strategy originates (Bonan et al., 2014). In CLM-ml v1, the model was altered to accommodate a continuum of stomatal behavior. In CLM-ml v1's revised formulation, stomatal conductance decreases from a maximum value as ψ_l decreases using the function:

$$f(\psi_l) = [1 + (\psi_l/\psi_{50})^{\alpha}]^{-1} \quad (5)$$

where ψ_{50} (MPa) is leaf water potential at 50% loss of conductance and α is a shape parameter for stomatal closure. In CLM-ml v1, ψ_{50} =

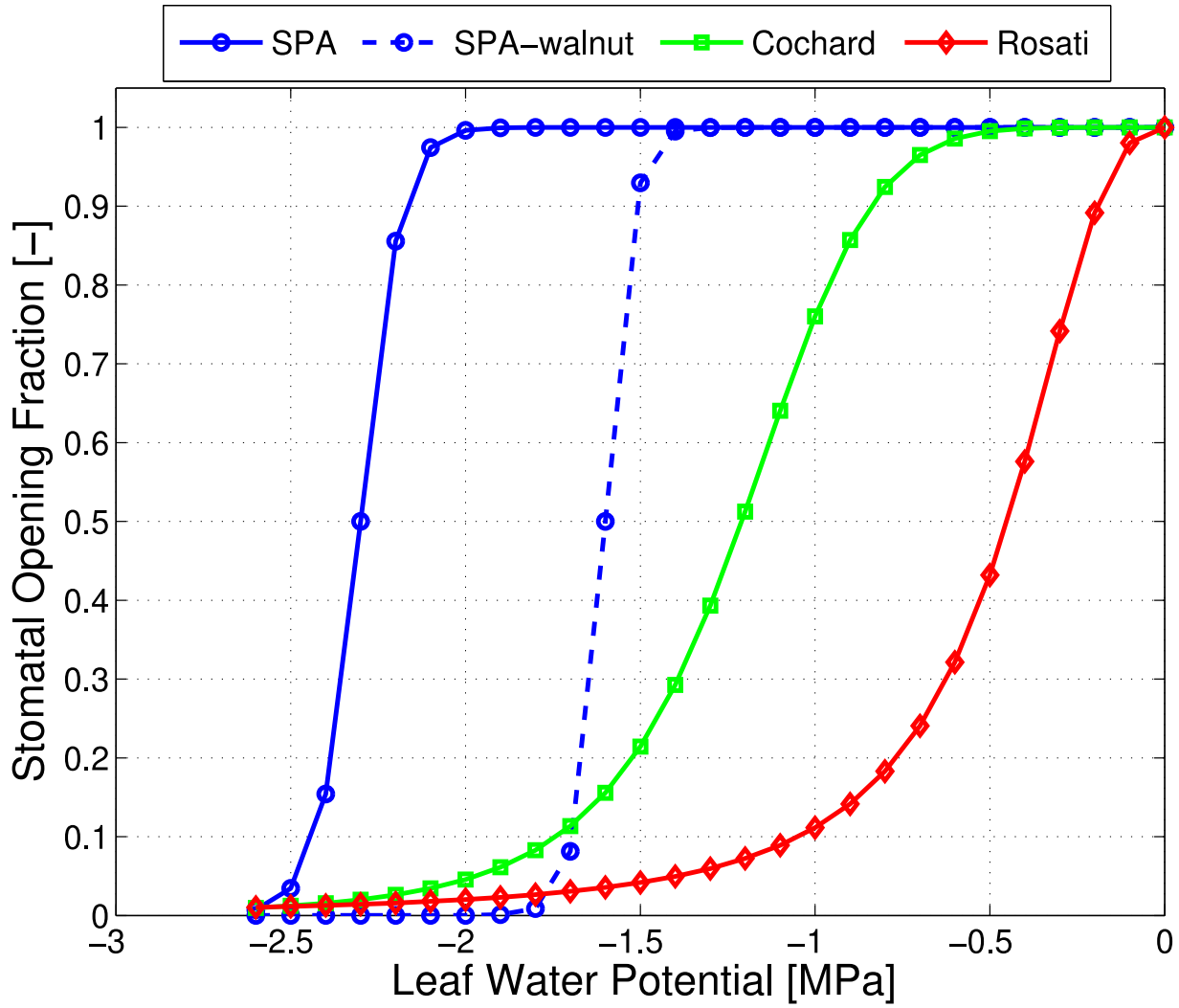

Fig. 7. Relative stomatal opening ($f(\psi_l)$; dimensionless denoted by –) in relation to leaf water potential (ψ_l) as specified with Eq. (5), where a value of 0 is fully closed and 1 is fully open. Bonan et al. (2021) used $\psi_{50} = -2.3$ MPa and $\alpha = 40$ in CLM-ml v1 to produce an abrupt decline in stomatal conductance as in SPA. Fitted parameter values for *Juglans regia* are $\psi_{50} = -0.45$ MPa and $\alpha = 2.60$ (Rosati et al., 2006) and $\psi_{50} = -1.21$ MPa and $\alpha = 6.05$ (Cochard et al., 2002). We use $\psi_{50} = -1.6$ MPa and $\alpha = 40$ to mimic the SPA stomatal physiology applied to walnut.

−2.3 MPa and $\alpha = 40$ (Bonan et al., 2021), which produces abrupt stomatal closure between $\psi_l = -2$ and −2.5 MPa to mimic the SPA implementation (Fig. 7).

Studies of leaf gas exchange show that photosynthesis, transpiration, and stomatal conductance decrease when walnut leaves are water-stressed, but the exact dependence of stomatal conductance on ψ_l is uncertain. Rosati et al. (2006) measured stomatal conductance in relation to stem water potential (see their Fig. 6). The parameter values obtained by fitting the observations to Eq. (5) are $\psi_{50} = -0.45$ MPa and $\alpha = 2.60$ ($N = 20$, $R^2 = 0.826$), in which stomatal conductance is about 10% of its maximum value at −1 MPa (Fig. 7). Measurements by Cochard et al. (2002, their Fig. 6) of potted *Juglans regia* × *nigra* find that stomata close to maintain leaf water potential above −1.6 MPa, with fitted parameters $\psi_{50} = -1.21$ MPa and $\alpha = 6.05$ ($N = 60$, $R^2 = 0.338$). Other studies report water-stressed leaf water potential equal to approximately −1.5 to −1.7 MPa for walnut (McElrone et al., 2010; Sun et al., 2011; Jerszurki et al., 2017; Calvo et al., 2023). Tyree et al. (1993) measured leaf water potential of −1.9 MPa at mid-day for drought-stressed *Juglans regia* grown in pots compared with −0.7 MPa with irrigation. The high water potential at stomatal closure reported by Rosati et al. (2006) is inconsistent with these low leaf water potentials; however, the data in Cochard et al. (2002) are for young potted plants, are not the Chandler variety, and have considerable scatter. Lacking definitive data to the contrary, we retain the functionality of the SPA stomatal response to ψ_l but with $\psi_{50} = -1.6$ MPa and $\alpha = 40$ (Table 2), which produces a sharp decline in stomata conductance at ψ_l between −1.5 and −1.8 MPa (Fig. 7).

Plant hydraulics. Tyree et al. (1993) reported a stem hydraulic conductance (k_p; per unit leaf area) equal to 7 mmol H_2O m^{-2} s^{-1} MPa^{-1} for *Juglans regia*, which is larger than the $k_p = 4$ used for broadleaf deciduous trees in previous simulations with CLM-ml v1 (Table 2). Studies of walnut found approximately equal root and stem conductance (Tyree et al., 1994), and we correspondingly decrease root hydraulic resistivity (R_r^*) to 14 MPa s g $mmol^{-1}$ H_2O from a prior value of 25.

Vegetation optics. Leaf optical properties are updated from the CLM-ml v1 values for broadleaf deciduous trees to values for *Juglans regia* (Table 2) as provided in the synthesis review of Majasalmi and Bright (2019). In their review of the literature, Majasalmi and Bright (2019) report walnut leaf reflectance (ρ_{leaf}) and leaf transmittance (τ_{leaf}) from two separate datasets. We use the average of the two datasets. Compared to the previous values, ρ_{leaf} decreases by 0.04 in the visible (VIS) and 0.03 in the near-infrared (NIR); τ_{leaf} decreases by 0.01 (VIS) and increases by 0.18 (NIR). Majasalmi and Bright (2019) report bark reflectance for

eight species of broadleaf deciduous tree, but not walnut. For lack of better information, we use the average values for broadleaf deciduous trees as recommended by Majasalmi and Bright (2019). Compared to the previous values, stem reflectance (ρ_{stem}) increases by 0.05 (VIS) and 0.10 (NIR). Majasalmi and Bright (2019) classified *Juglans regia* foliage as having a planophile leaf angle distribution (i.e., most leaves oriented in the horizontal plane), based on original data from Chianucci et al. (2018). Using the two-parameter beta distribution as described in Table 2 of Chianucci et al. (2018), the planophile leaf angle distribution has an inclination index (χ_l), which quantifies the departure from a spherical distribution, equal to 0.53. This is more horizontal than the value used previously. It is notable that the values for walnut leaves are not very different from the generic values for temperate broadleaf deciduous trees proposed by Majasalmi and Bright (2019): ρ_{leaf}, 0.08 (VIS) and 0.42 (NIR); τ_{leaf}, 0.06 (VIS) and 0.43 (NIR); χ_l, 0.59.

2.2.4. Model simulations

Meteorological forcing data are prepared for May 2007 using the CHATS measurements. The observations at the 23-m level (taken as the forcing height in the model) used as input to the model are horizontal wind speed, air temperature, and relative humidity. Additional observations are barometric pressure (1 m), precipitation (1 m), and incoming shortwave and longwave radiation (16 m). Missing data are gap-filled using two methods: (1) if the gap is for a short time, linear interpolation (in time) is used to fill the missing period, or (2) the gap is filled by alternative sensors located near the missing level. Forcing data for April (needed for CLM5 simulations as described below) are also prepared, but precipitation measurements are missing over a multiday period. There are several sites in the California Irrigation Management Information System (CIMIS) that are within about 30 km of the walnut orchard (Davis, Winters, and Dixon stations) and that data show zero precipitation during the missing data gap. Atmospheric CO_2 concentration is required for the photosynthesis and stomatal conductance calculations and is set to 383 ppm, which is representative of 2007 (Meinshausen et al., 2017).

We test CLM-ml in an off-line form decoupled from CLM5 as in Bonan et al. (2018, 2021). In addition to the meteorological forcing, this configuration requires three additional input data streams (provided by CLM when coupled): (1) a time series of leaf area index and stem area index (described in Section 2.2.2); (2) a soil moisture dataset, which specifies soil moisture for each soil layer at every model timestep; and (3) initial soil temperatures (thereafter, soil temperatures are calculated using one-dimensional (vertical) heat transfer equations as part of the multilayer canopy energy budget).

Soil moisture and temperature were measured at 5-cm depth during CHATS, but CLM-ml requires a vertical profile as in CLM5. We use CLM5 to obtain the soil moisture and temperature profiles. We use the same protocol as the tower simulations reported by Lawrence et al. (2019), but for the walnut orchard. We spin-up CLM5 using meteorology from the Global Soil Wetness Project Phase 3 for 1995–2007. The initial condition file for 1 April 2007 is used with CHATS-specific meteorology to simulate 1 April–31 May 2007. CLM5's irrigation scheme (needed to mimic the observed irrigation) produces soils that are too wet compared with the observations. Consequently, we adjust the moisture content of the first three soil layers (at depths of 1, 4, and 9 cm) to match the CHATS observations (Fig. S.9). Initial soil temperatures are taken from the CLM5 simulation. For convenience, the three data streams of leaf and stem area index, soil moisture, and initial soil temperature are obtained during the CLM-ml simulations by reading a CLM5 model output file.

Model simulations are performed for May with a vertical resolution $\Delta z = 50$ cm (Bonan et al., 2021). To determine the impact of parameter selections on model results, several sensitivity studies are conducted testing parameter values used in the model. We examine the walnut physiology parameters in Table 2. We vary V_{cmax25} between 50 and 150 μmol m^{-2} s^{-1} and ι between 300 and 800 μmol CO_2 mol^{-1} H_2O. We test the four leaf water potential relationships shown in Fig. 7. We vary k_p between 3 and 9 mmol H_2O m^{-2} s^{-1} MPa^{-1} and R_r^* between 10 and 28 MPa s g $mmol^{-1}$ H_2O. We examine the sensitivity to the default and revised leaf optical parameters shown in Table 2. We vary c_d between 0.15 and 0.4. We also examine the sensitivity to two key model assumptions: (1) We vary the upper constraint for L_c/L from the default value of one. (2) We test the impact of setting soil moisture to the CHATS observations by varying the depth to which the observations are applied.

3. Results

3.1. Canopy fluxes

Fig. 8 shows net radiation (R_{net}), sensible heat flux (H), latent heat flux (λE), and friction velocity (u_*) above the canopy for an example four days in May. The observations are at 16-m height for R_{net}, 23-m height for H and λE, and 10-m height for u_*, and the model values are at the corresponding heights. The model closely reproduces the observations over the four days, though midday λE can be biased high. $\beta = u_*/U(h)$ compares favorably with the observations over the same four-day period (Fig. 9a).

Simulated R_{net}, H, λE, and u_* also compare favorably with the observations for the entire month of May. Fig. 10 shows the data binned and plotted in relation to the observed bulk Richardson (Ri_b) to assess model performance across strongly unstable (SU), weakly unstable (WU), near-neutral (NN), weakly stable (WS), and strongly stable (SS) regimes. R_{net}, H, and u_* are well-simulated in all stability regimes. λE is biased high in strongly and weakly unstable conditions but corresponds well with the observations in near-neutral and stable conditions. The variability in the measurements among time samples within the Ri_b bins is also well simulated (Fig. S.10).

The model predicts β reasonably well compared to observations across all stability regimes throughout May (Fig. 9b,c). The largest biases occur in the stable regime with $Ri_b > 1$, but there are few observations for comparison with the model. The model assumes a neutral value $\beta_N = 0.35$, which corresponds with the observations for near-neutral conditions ($-0.01 \le Ri_b \le 0.01$). The functional form of Eq. (2) is evident in the decline in β in the strongly unstable regime ($Ri_b \le -0.1$).

Displacement height (d) is derived from the Harman and Finnigan (2007, 2008) roughness sublayer theory. The simulated d corresponds closely with d derived from the observations (Fig. 11). Displacement height varies with flow, with largest values in strongly stable conditions.

Heat storage in the canopy compares well with the observations (Fig. 12). The observed heat storage in the canopy air ranges from ±40 W m^{-2} depending on time of day. The model produces a similar range of heat storage. Heat stored in the leaves is minor.

Table 3 shows components of the surface energy balance averaged for daytime and nighttime. Differences in R_{net} from the observations are –27.7 W m^{-2} averaged during daytime (10:00–14:00 PST) and 1.6 W m^{-2} at night (00:00–04:00 PST). Daytime biases in H and λE are 24.7 and 70.6 W m^{-2}, respectively. These biases are small compared to the lack of energy closure in the observations. The mean observed R_{net} is 669 W m^{-2} during the day, and the observed energy imbalance is 183 W m^{-2}. Daytime heat storage in the canopy air space and loss of heat at night are well replicated by the model. The daytime bias in u_* is small (–0.01 m s^{-1}), but the model overestimates u_* at night (0.07 m s^{-1}) consistent with the high bias in weakly stable conditions (Fig. 10e).

The model overestimates soil heat flux during daytime (Table 3). Further analysis of soil heat flux over a four-day period suggests that the observations are not representative of the larger tower footprint. Direct sunlight regularly reaches the ground in the afternoon, as seen

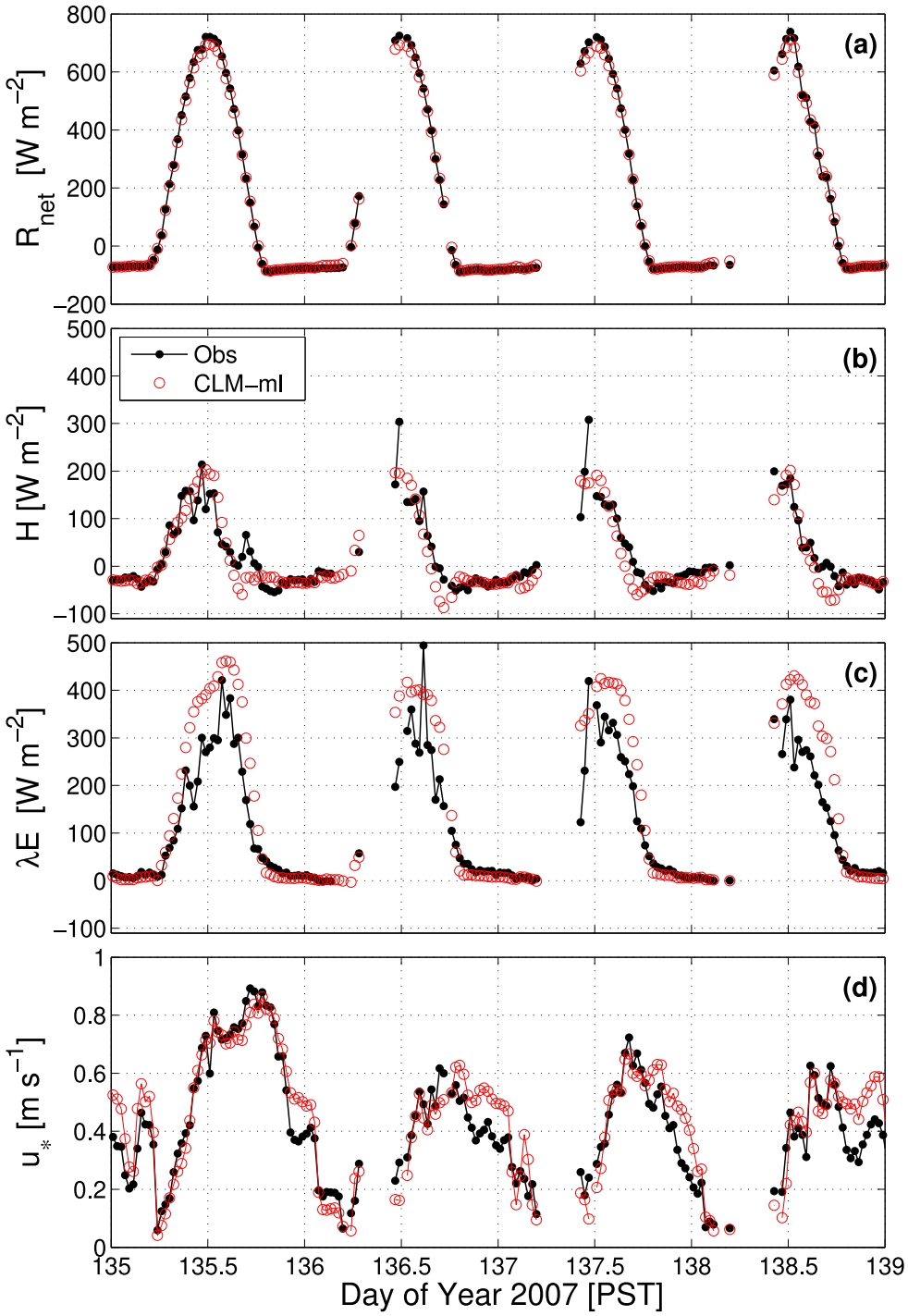

Fig. 8. Time series of 30-min mean above-canopy (a) net radiation (R_{net}), (b) sensible heat flux (H), (c) latent heat flux (λE), and (d) friction velocity (u_*) for the observations and CLM-ml (see legend in (b)). The observation heights are 16-m for R_{net}, 23-m for H and λE, and 10-m for u_*. Model values are at the corresponding heights. Gaps in the data arise from filtering of northerly winds.

in large spikes in 2-m R_{net}, which suggests the sensor may have been shaded at other times of the day (Fig. S.11a). The spikes in R_{net} correspond with the time when the observed soil heat flux peaks (Fig. S.11b) and the soil is warmest (Fig. S.11c). The model does not replicate the spikiness in the R_{net} measurements, and soil heat flux peaks earlier in the day compared with the observations. The model soil temperatures at 4 cm and 9 cm are warmer than the observed temperatures at 5 cm depth (Fig. S.11c).

3.2. Scalar profiles

Fig. 13 shows vertical profiles of observed and simulated air temperature, specific humidity, and wind speed within and above the canopy stratified by stability class. The observations show a weak decrease in air temperature between the ground and 23-m height during unstable conditions (1 °C) and a near-constant temperature profile during neutral regimes (Fig. 13a,b). The model generally reproduces the observed profiles. The model predicts significantly biased profiles during strongly

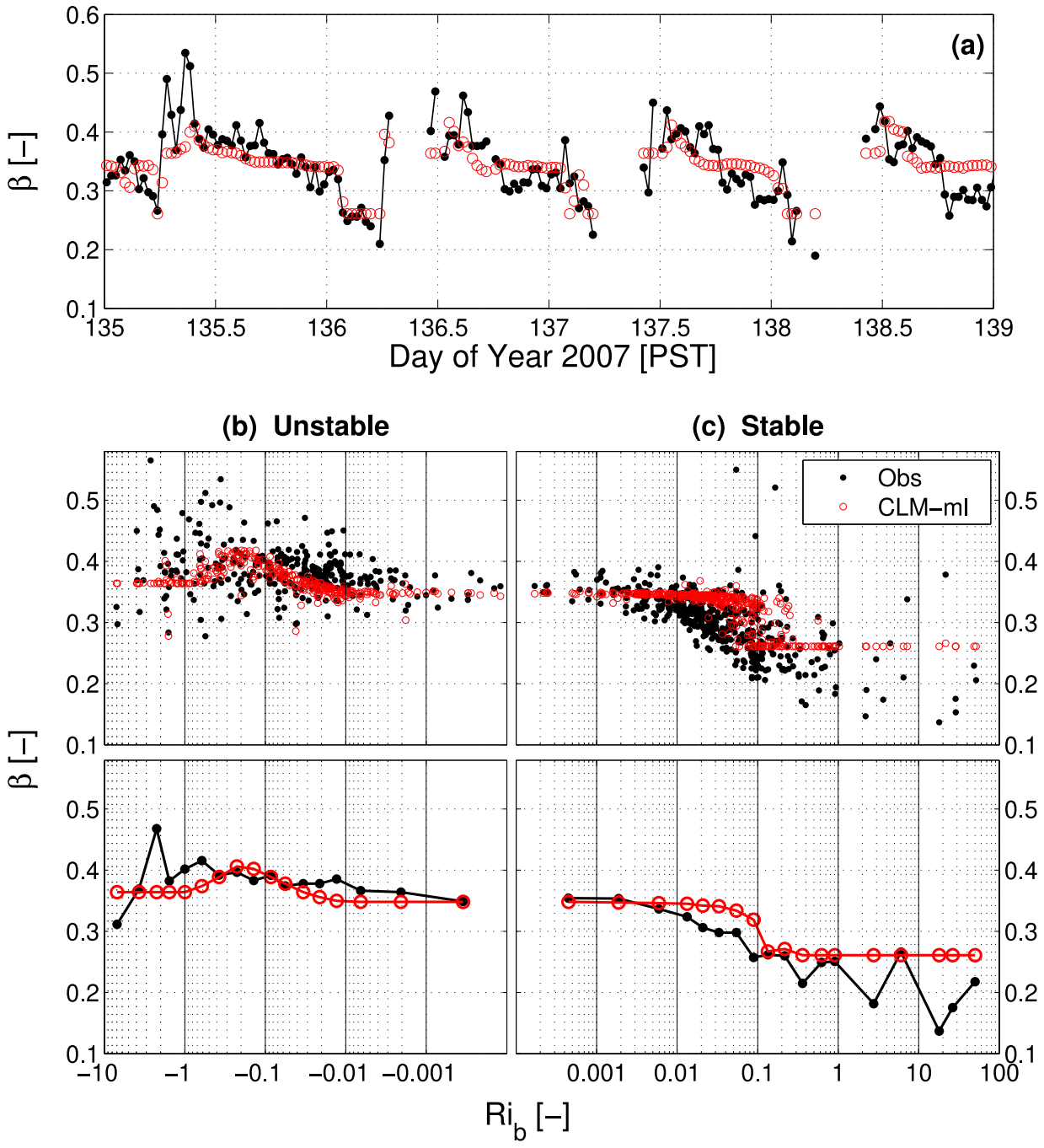

Fig. 9. (a) Time series of 30-min mean β, which is the ratio of friction velocity (u_* at 10-m) to mean horizontal wind speed at the canopy top ($U(h)$) and is dimensionless (denoted by –), for the observations and CLM-ml (see legend in (c)). The lower panels show β as a function of the observed bulk Richardson (Ri_b), which is dimensionless (denoted by –), for the month of May during (b) unstable and (c) stable atmospheric conditions. In (b) and (c), the upper panels depict every 30-min value, and the lower panels present bin averages that are defined logarithmically to adequately sample the range of Ri_b.

stable conditions, when the near-ground air is several degrees too warm compared with the observations. The observations show a well-mixed air space below 7.5 m, whereas the model simulates a large gradient in air temperature.

Observed specific humidity generally decreases by 0.5–1 g kg^{-1} between the ground and 23-m height in all stability conditions (Fig. 13c,d). The model shows similar behavior, though it is consistently biased low by a few tenths g kg^{-1}. Under strongly stable conditions, the bias in specific humidity follows a similar pattern as air temperature near the ground.

Lack of mixing under the canopy during strongly stable conditions is seen in the aerodynamic conductance, which governs turbulent transport of heat and moisture vertically between levels. The conductance frequently attains low values (equivalent to a resistance of 500 s m^{-1}, which is the limit shown in Table 1) in the lower canopy (≤4 m) at night (Table S.3). The limit is never reached during daylight hours

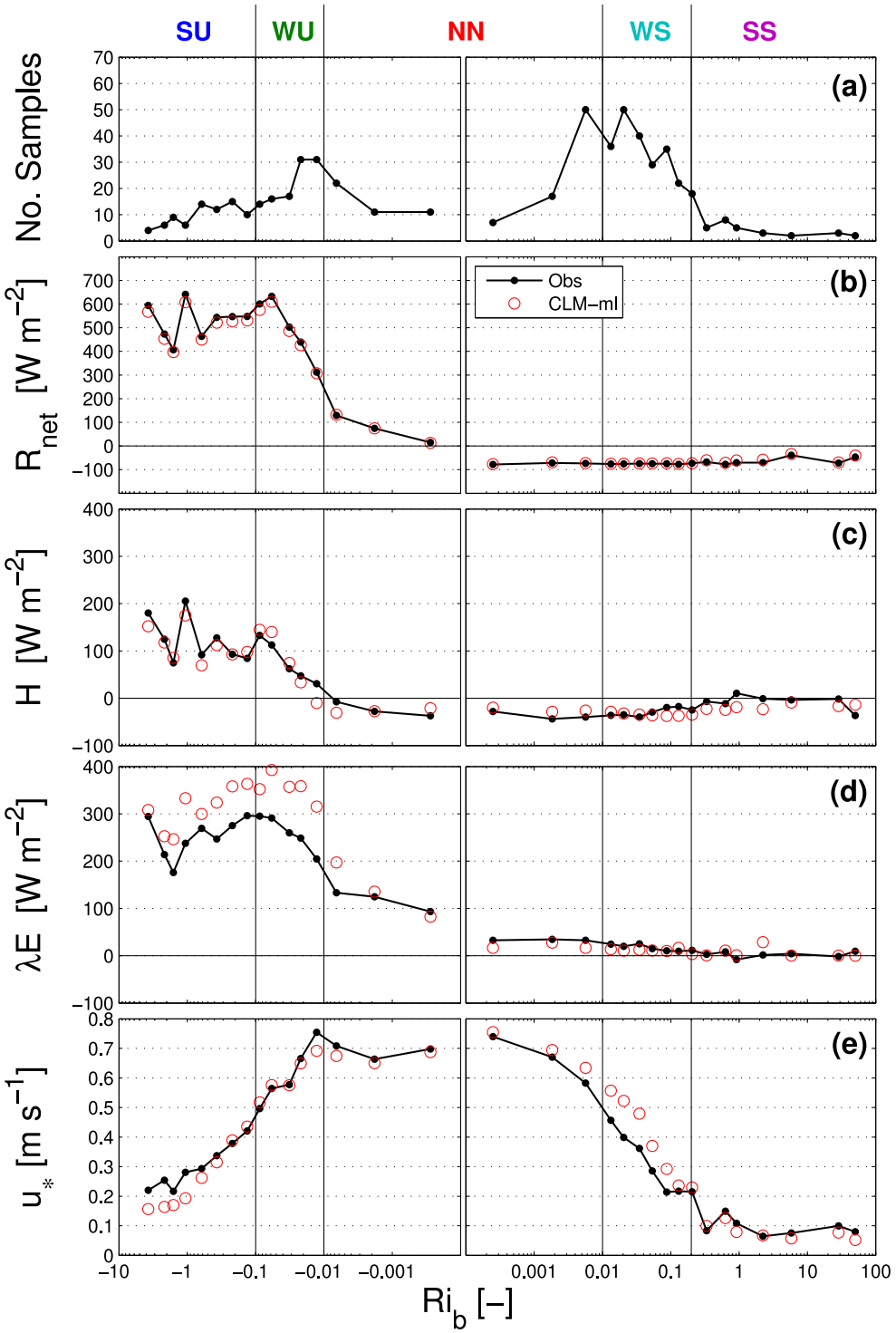

Fig. 10. The above-canopy 30-min mean values from May 2007 of (b) net radiation (R_{net}), (c) sensible heat flux (H), (d) latent heat flux (λE), and (e) friction velocity (u_*) binned by the observed bulk Richardson number (Ri_b). These are mean statistics for both the observations and CLM-ml and the legend in (b) applies to all panels. The observation and model heights are the same as in Fig. 8. The number of 30-min samples within each bin is shown in (a). The Ri_b region used for each stability class is indicated by the colored text and vertical lines. The five Ri_b ranges selected for analysis are: SU (strongly unstable), WU (weakly unstable), NN (near-neutral), WS (weakly stable) and SS (strongly stable).

(08:00–16:00 PST) at any level and is never reached at heights >4 m at any time.

Wind speed is well simulated during all stability regimes (Fig. 13e,f). The greatest within-canopy wind speed attenuation occurs during weakly unstable, near-neutral, and weakly stable regimes. The model replicates the strong reduction of wind speed, as well as the weaker attenuation during the strongly unstable and strongly stable regimes. The model does not capture the secondary wind maximum in the understory seen in the observations. Wind speed is commonly less than 0.04 m s^{-1} below 6 m height during the night (Table S.4). This is the wind speed at which the imposed minimum leaf boundary layer conductance is attained (0.2 mol m^{-2} s^{-1}, equivalent to a resistance

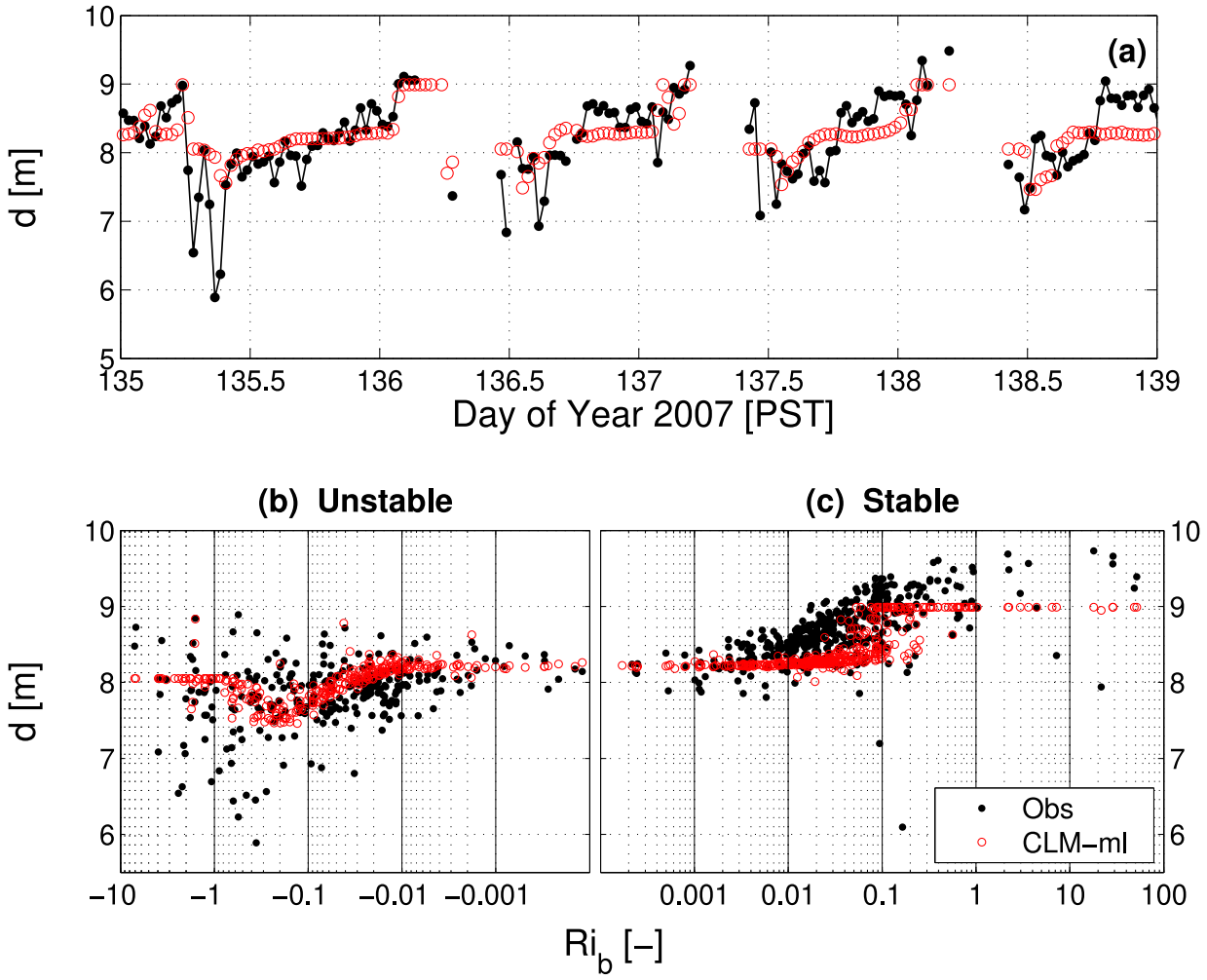

Fig. 11. (a) Time series of 30-min mean displacement height (d) for the observations and CLM-ml (see legend in (c)). The lower panels show d as a function of the observed bulk Richardson (Ri_b) for the month of May during (b) unstable and (c) stable atmospheric conditions.

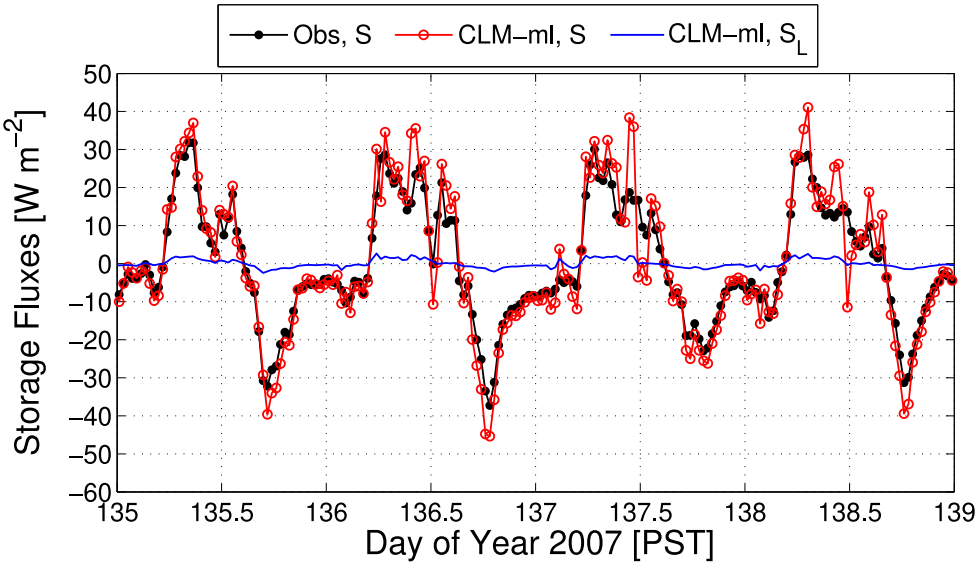

Fig. 12. Time series of 30-min mean observed and CLM-ml heat storage (S) within the air space below 23 m. Air heat storage is the combined sensible and latent heat storage terms. Also shown is the model heat storage in leaf biomass (S_L).

Table 3
Daytime and nighttime mean ± standard deviation for May 2007 of both the observations and CLM-ml and the difference between them. The number of 30-min samples (N) used to calculate the statistics is shown out of the 248 possible samples. Units are [W m^{-2}] for fluxes and [m s^{-1}] for friction velocity. Height is in [m]. Net radiation is positive towards the surface. Sensible and latent heat fluxes are positive in the upward direction. Soil heat flux is positive into the soil. Air heat storage is the combined sensible and latent heat storage terms. The overall energy balance is $R_{net} - G - S - S_L = H + \lambda E$. Residual energy is the energy imbalance.

Variable	Symbol	Height	Daytime (10:00–14:00 PST) [N = 99 of 248]			Nighttime (00:00–04:00 PST) [N = 130 of 248]		
			Observations	CLM-ml	Model−Obs	Observations	CLM-ml	Model−Obs
Friction velocity	u_*	10	0.46 ± 0.17	0.45 ± 0.20	−0.01 ± 0.06	0.31 ± 0.17	0.37 ± 0.20	0.07 ± 0.08
Net radiation	R_{net}	16	668.8 ± 101.8	641.1 ± 93.2	−27.7 ± 11.9	−74.6 ± 8.9	−73.0 ± 9.5	1.6 ± 5.1
Sensible heat flux	H	23	124.1 ± 74.7	148.8 ± 62.5	24.7 ± 52.8	−25.4 ± 20.5	−31.7 ± 11.8	−6.3 ± 18.5
Latent heat flux	λE	23	331.8 ± 103.9	402.5 ± 69.4	70.6 ± 76.7	10.3 ± 10.8	5.0 ± 5.0	−5.4 ± 8.5
Soil heat flux	G	0	22.4 ± 7.8	82.7 ± 19.3	60.3 ± 18.5	−20.2 ± 5.4	−39.5 ± 6.2	−19.3 ± 4.0
Air heat storage	S	0–23	7.7 ± 6.9	6.7 ± 11.1	−1.0 ± 7.7	−5.5 ± 4.0	−6.2 ± 5.4	−0.7 ± 3.6
Leaf heat storage	S_L	0–10	–	0.4 ± 0.6	–	–	−0.5 ± 0.7	–
Residual energy	–	–	182.7	0.0	–	−33.9	0.0	–

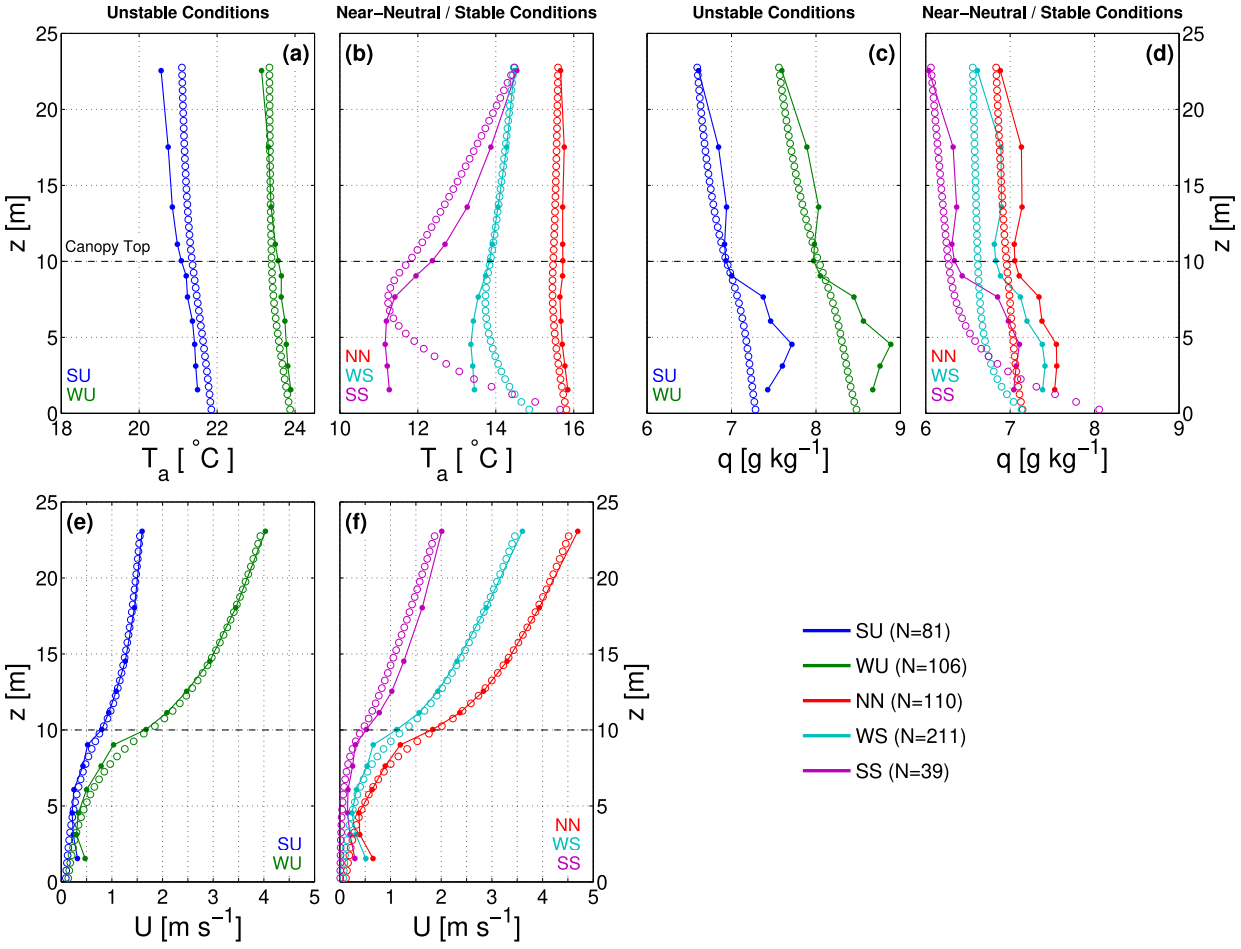

Fig. 13. The mean vertical scalar and wind profiles from May 2007 of (a,b) air temperature (T_a), (c,d) specific humidity (q), and (e,f) horizontal wind speed (U). The observations are solid circles and CLM-ml results are open circles. The canopy height is 10 m as indicated by the horizontal dashed line. The data have been separated into different stability classes, where the left-hand panels are strongly unstable (SU) and weakly unstable (WU) and right-hand panels are near-neutral (NN), weakly stable (WS), and strongly stable (SS) atmospheric conditions. Each stability class is plotted in a different color as specified in the legend which includes the number (N) of 30-min samples within each class.

of 211 s m^{-1}; Table 1). Low wind speeds are especially prevalent in strongly stable conditions (Fig. 13f).

3.3. Flux profiles

Fig. 14 shows vertical profiles of observed and simulated R_{net}, H, and λE stratified by stability class. The magnitude of the fluxes and the shape of the profiles vary depending on the stability regime, and the model generally simulates similar profiles. Simulated R_{net} is similar to the observations at 16 m and 2 m (Fig. 14a,b). The observations show that H increases with height above the ground in the canopy and is near constant with height above the canopy during unstable conditions (Fig. 14c). The model replicates the profile. There is generally a small source of heat (positive H) in the lower canopy and a sink of heat (negative H) in the upper canopy in stable conditions (Fig. 14d). Similar behavior is seen in the model. λE increases with height above

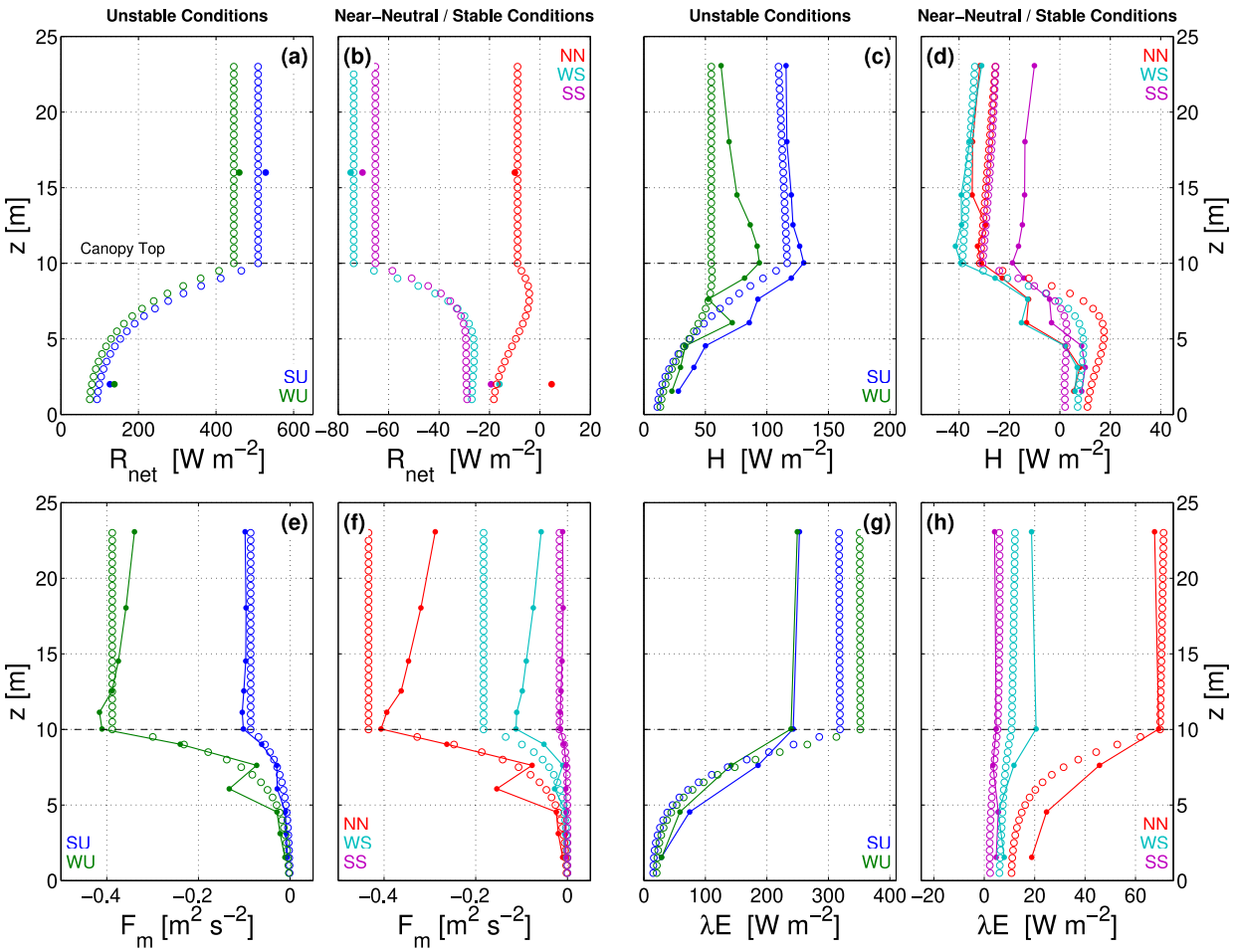

Fig. 14. As in Fig. 13, except the variables plotted are (a,b) net radiation (R_{net}), (c,d) sensible heat flux (H), (e,f) momentum flux ($F_m = -[\overline{u'w'}_z^2 + \overline{v'w'}_z^2]^{\frac{1}{4}}$), and (g,h) latent heat flux (λE).

ground in the canopy during unstable and near-neutral conditions and is nearly invariant with height during stable conditions (Fig. 14g,h). The model produces a similar evolution of the λE profile with height, but the model's high bias at canopy top during unstable conditions is clearly evident.

Momentum absorption increases with height above the ground (Fig. 14e,f). The model produces similar profiles. Momentum absorption by the canopy is largest during weakly unstable and near-neutral conditions. Less momentum attenuation occurs during strongly unstable and weakly stable regimes. The momentum flux is nearly invariant with height during strongly stable conditions.

3.4. Numerical methods

The combination of using a fourth-order Runge–Kutta (RK4) method with interpolation of the 30-min meteorological forcing to the 5-min timestep smooths the modeled fluxes compared with the original Euler method used in CLM-ml v1. Fig. 15a shows R_{net} over a 6.5-h period spanning late morning to afternoon. The data are plotted at 5-min intervals using the Euler method (as in CLM-ml v1), RK4, and RK4 with 5-min interpolation of the meteorological forcing. The Euler method produces a step-like time series for R_{net} because the meteorology is updated every 30-min. The RK4 without interpolation reveals a similar step-like time series. Allowing for interpolation temporally smooths R_{net}.

The Euler method produces a spiky time series of H (Fig. 15b). There is a period of adjustment in which H at the first 5-min timestep is substantially less than the values at subsequent timesteps. Thereafter, H can oscillate between high and low values. The RK4 without interpolation smooths the time series, but the initial flux adjustment remains. Interpolation further smooths the time series of H and eliminates the initial adjustment. The variability of the six 5-min values of H within a 30-min interval is reduced with RK4 and is further reduced with the interpolation (Fig. 15c). Another time period later in the month that spans morning to midday shows similar results (Fig. S.12).

Over the month of May, the three numerical methods produce similar mean diel cycles, though midday H is slightly reduced with the two RK4 methods (Fig. 15d). The RK4 methods reduce temporal variability in H within a 30-min interval compared with the Euler method (Fig. 15e). With RK4 and interpolation, the temporal variability is uniformly small at all times of day. In contrast, the Euler method and RK4 without interpolation show two peak periods of variability in the morning and evening.

3.5. Model sensitivity analysis

The plant physiology parameters for walnut (Table 2) reduce daytime biases compared with other parameter values and have little effect at night. Daytime results are particularly sensitive to the effect of leaf water potential on stomatal conductance. The SPA-walnut relationship (Fig. 7) provides close agreement with the observed above-canopy R_{net}, H, λE, and u_*, as well as the air temperature measurements (Fig. 16). The Cochard et al. (2002) and Rosati et al. (2006) relationships, in which stomata close at relatively high leaf water potential (Fig.

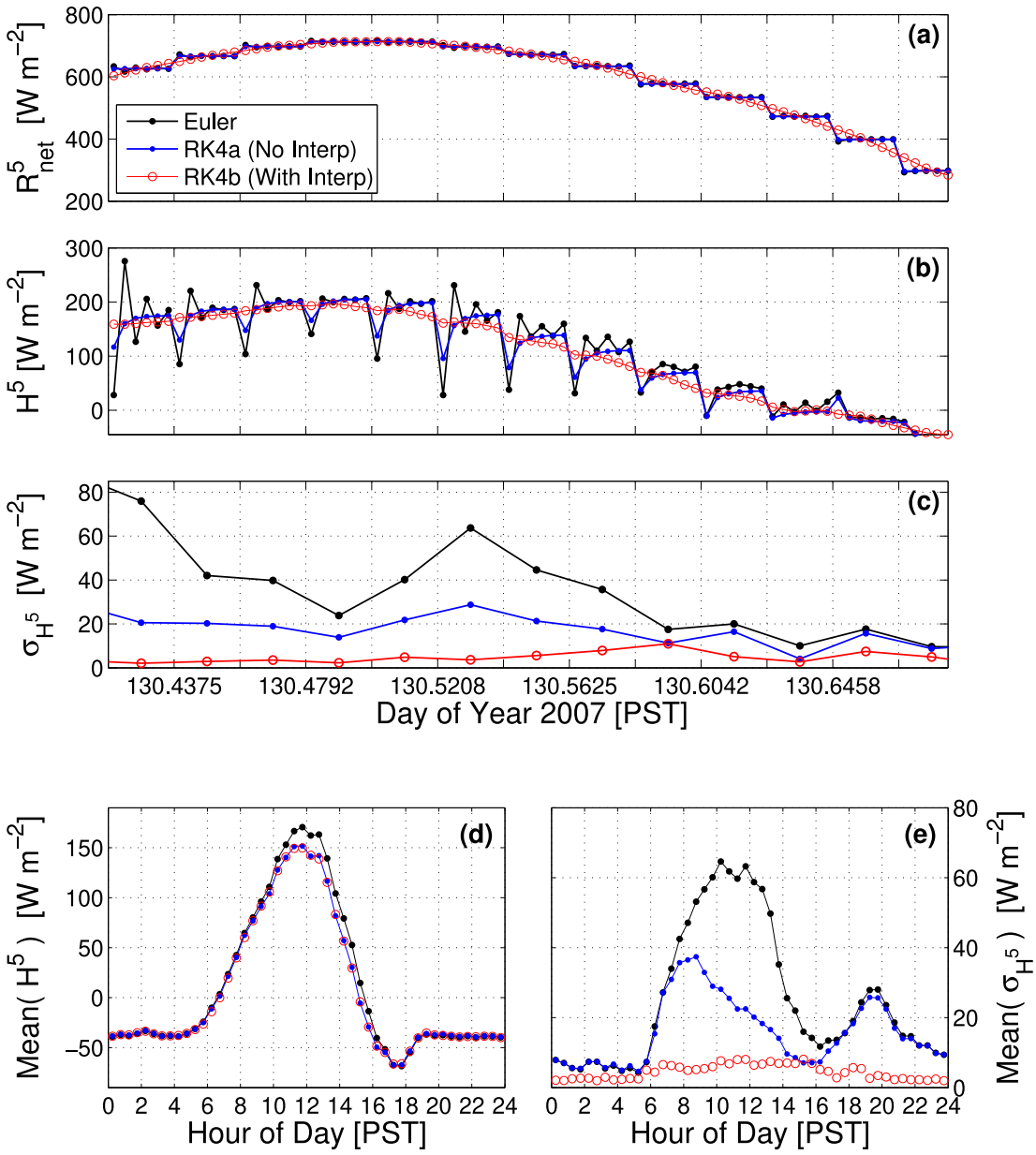

Fig. 15. Effect of numerical methods on model fluxes. The top two panels show (a) net radiation and (b) sensible heat flux over a 6.5-hour time period. Each data point is a 5-min flux (denoted as R^5_{net} and H^5, respectively), and there are six data points for each 30-min interval. The vertical lines mark the beginning of the 30-min interval. Shown are the Euler method used in CLM-ml v1, the fourth-order Runge–Kutta without interpolation of the meteorological forcing to 5-min (RK4a), and Runge–Kutta with interpolation (RK4b). Panel (c) shows the standard deviation of H^5 calculated with the six 5-min fluxes for each 30-min interval (denoted as σ_{H^5}). Panel (d) shows the mean diel cycle of sensible heat for May plotted at 30-min intervals (i.e., the mean of the six H^5 fluxes and averaged over May), and panel (e) is σ_{H^5} within each 30-min interval averaged over the month. The legend in (a) applies to all panels. Data are for CLM-ml only and have not been filtered for wind direction.

7), decrease λE, increase H, and warm the air compared with the observations (Fig. 16).

Daytime λE increases and H decreases with larger V_{cmax25}, with a slight cooling of air temperature (Fig. S.13). Larger ι produces the opposite behavior (Fig. S.14). The model values (Table 2) have low biases compared with the observations. The increase in stem hydraulic conductance (k_p) from 4 to 7 mmol H_2O m^{-2} s^{-1} MPa^{-1} (Table 2) makes it easier to transport water from the soil through the stems to leaves to sustain high latent heat flux. The effect of increasing k_p is similar to that of V_{cmax25} (Fig. S.15). The decrease in root hydraulic resistivity (R^*_r) from 25 to 14 MPa s g mmol^{-1} H_2O (Table 2) also makes it easier to transport water from the soil, but the model is comparatively insensitive to changes in R^*_r (Fig. S.16).

The revised vegetation optical parameters (Table 2) decrease daytime R_{net}, H, and λE compared with the CLM-ml v1 values and reduce the bias compared with observations (Fig. S.17). There is little difference between the generalized values for broadleaf deciduous trees given by Majasalmi and Bright (2019) and the walnut-specific values.

Model results are relatively insensitive to the specific depth to which the CHATS observed 5-cm soil moisture is applied, so long as within the top 16 cm, but daytime λE declines, H increases, and the canopy air warms if the observed near-surface soil moisture is applied to deeper soil layers (Fig. S.18). In the model, 50% of the roots are in the top 16 cm of soil, 67% are in the top 26 cm, and 96% are in the top 80 cm.

Above canopy energy fluxes are relatively invariant to c_d, but not so for u_* and air temperature (Fig. 17). u_* decreases with higher values of c_d, and $c_d = 0.25$ minimizes the bias during the day (but not at night).

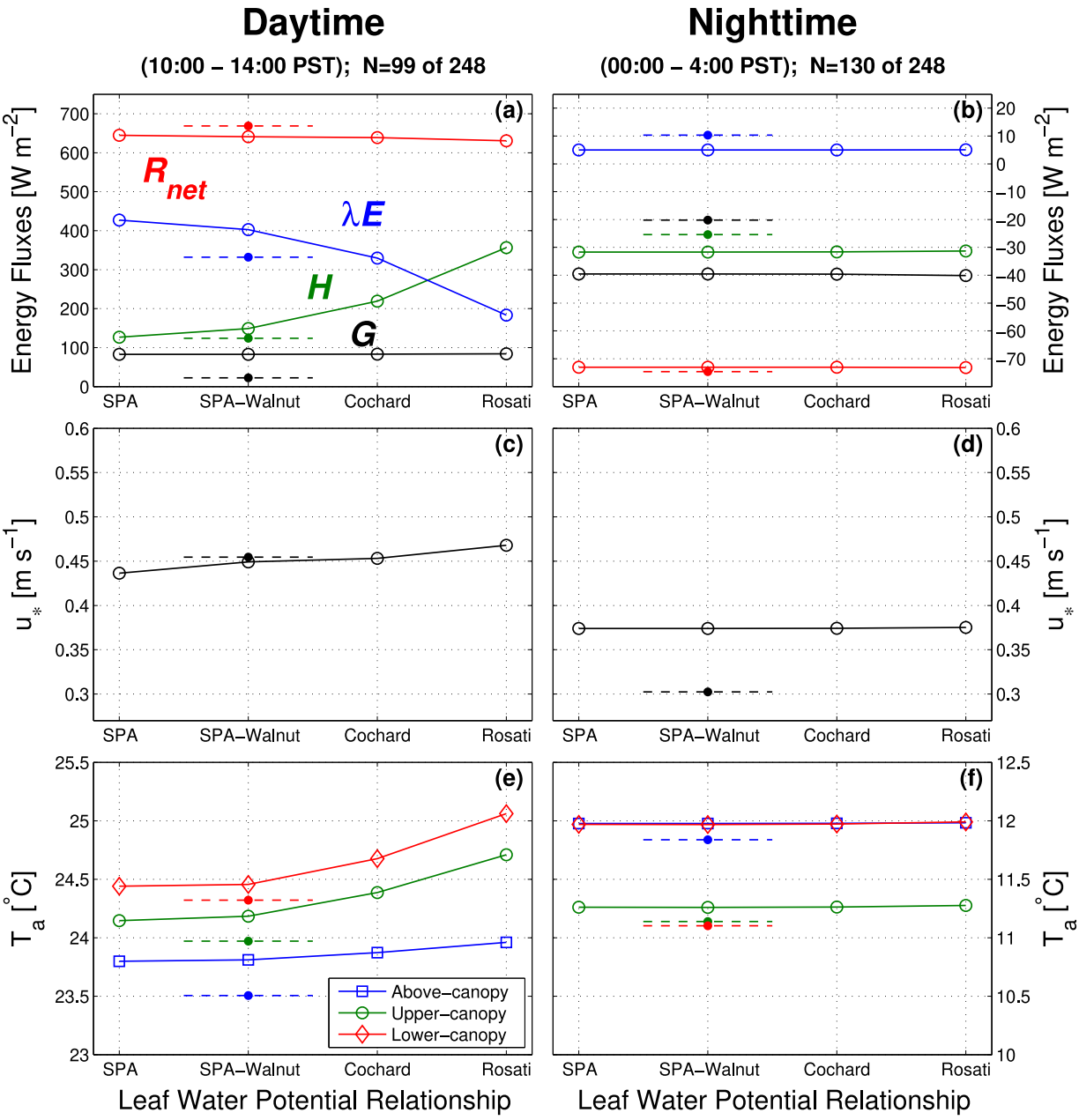

Fig. 16. Model sensitivity results to the four $f(\psi_l)$ functions shown in Fig. 7. Shown are mean values during the (left panels) daytime (10:00–14:00 PST) and (right panels) nighttime (00:00–04:00 PST) of: (a,b) above-canopy net radiation (R_{net}), sensible heat flux (H), latent heat flux (λE), and soil heat flux (G), (c,d) 10-m friction velocity (u_*), and (e,f) air temperature (T_a) at three different heights (see legend). Closed circles are observations, which are shown at the default model configuration. Open symbols are model results. The number of 30-min samples (N) used to calculate the statistics is shown out of the 248 possible samples.

Daytime temperatures within the canopy increase with larger c_d, and $c_d = 0.25$ has low bias. At night, c_d has a large effect on the temperature of the upper canopy.

The restriction $L_c/L \leq 1$ (Table 1) is most consequential at night and has little effect during daytime hours (Fig. S.19). In particular, u_* decreases and the air becomes colder (especially in the upper canopy) as L_c/L is allowed to become larger (i.e., the atmosphere is allowed to become more stable so that L becomes increasingly large and positive).

4. Discussion

For the month of May 2007, the model successfully replicates most of the variation across atmospheric stability regimes in β (Fig. 9) and R_{net}, H, λE, and u_* measured above the canopy (Fig. 10), as well as profiles of within- and above-canopy air temperature, specific humidity, and wind speed (Fig. 13) and turbulent fluxes (Fig. 14). The temperature and humidity profiles during strongly stable conditions reveal the model's primary deficiency. The model-data comparisons provide guidance for: the observations needed to assess the accuracy of and inform further research needs for multilayer canopy models; soil measurements to constrain models; and parameter estimation. In the discussion of modeling needs that follows, we contrast parameterizations used in CLM-ml v2 with similar parameterizations in CLM5/6.

4.1. Canopy turbulence

Wind speed in the canopy (Fig. 13e,f) follows the well-known exponential profile obtained as an analytical solution to the one-dimensional (vertical) momentum conservation equation (e.g., Cionco, 1965). The exponential decay coefficient (the parameter a in Cionco, 1965, his

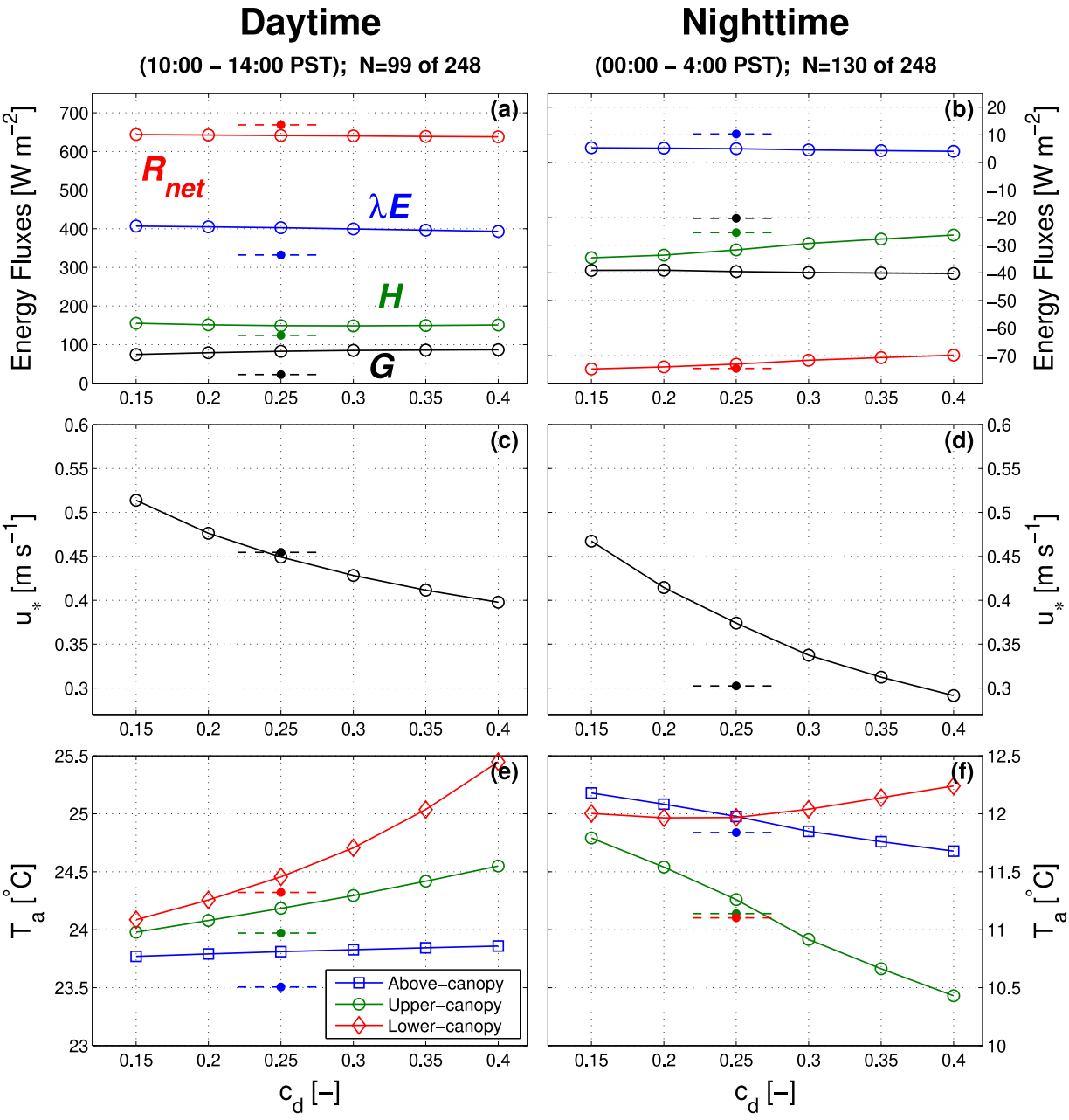

Fig. 17. As in Fig. 16, but for variation of the canopy element drag coefficient (c_d).

Eq. 4) varies with canopy structure and has been obtained by fitting the equation to measurements (Cionco, 1978; Thom, 1975; Brutsaert, 1982). In CLM-ml v2, Cionco's (1965) a is obtained from roughness sublayer theory that links the above- and within-canopy wind profiles (Harman and Finnigan, 2007). The parameter (see Bonan et al., 2018, their Eq. 21) relates to the dominant scale of shear-driven turbulence generated at or near the top of the canopy and is equal to the vorticity thickness $\delta_\omega = U/(\partial U/\partial z)$ of the turbulent eddies generated through an inflection-point instability at canopy top ($z = h$, see Raupach et al., 1996; Finnigan et al., 2009). By definition, the assumed exponential wind profile (or first-order closure approximation) cannot capture the observed secondary wind speed maximum near the ground, but the error is small compared with the in-canopy wind speed reduction arising through the action of canopy drag.

The wind profile has important consequences for leaf source/sink fluxes. During daytime, leaves high in the canopy receive high radiation loading, but are exposed to relatively high winds compared to lower in the canopy. The high leaf boundary layer conductance means that it is easy to transport heat away from the leaves. Leaves deeper in the canopy receive less radiation but are exposed to lower wind speed and have lower boundary layer conductance. The decline in wind speed from 1 m s^{-1} in the upper canopy to 0.2 m s^{-1} in the understory decreases leaf boundary layer conductance from 1.0 to 0.4 mol m^{-2} s^{-1} (25 °C air temperature, 4 cm leaf dimension). Few studies have measured vertical variation in leaf boundary layer conductance, but observations in an Amazon rainforest found a decline from 1.4 mol m^{-2} s^{-1} at the top of the canopy to 0.9 in the lower canopy and 0.2 at the forest floor (Roberts et al., 1990).

CLM5/6, in contrast, has a big-leaf canopy. Wind speed in the canopy (U_{af}) is taken to be equal to friction velocity (see Lawrence et al., 2018, their Eq. 2.5.117). The approximation originates from Deardorff (1978, see his Eq. 20), who set wind speed in a dense canopy to $U_{af} = 0.83u_*$. In developing the Biosphere–Atmosphere Transfer Scheme (BATS), Dickinson (1984) revised the expression to $U_{af} = u_*$

(see his Eq. 8b) and stated that it "is of adequate accuracy for the present model". U_{af} is used in CLM's calculation of leaf boundary layer conductance (see Lawrence et al., 2018, their Eq. 2.5.122).

Air temperature has small vertical variation during unstable and near-neutral conditions at the walnut orchard (Fig. 13a,b), which likely results from the relatively sparse canopy and the ability for a portion of the insolation to reach the ground. CLM-ml v2 replicates these profiles. Dense leafy forests with a more closed canopy can have more complex profiles with a mid-canopy thermal maximum in the afternoon, which the model also replicates (Wozniak et al., 2020; Bonan et al., 2021). However, our analysis stratifying the results by atmospheric stability emphasizes a well-known limitation of the model's assumed first-order closure formulation of in-canopy mixing (Fig. 13b). Under nighttime weak winds, radiative cooling of the uppermost leaves cools the air in contact with them. In the field, this cool upper-canopy air sinks while the warmer near-surface air rises which homogenizes canopy air temperature. The model's simplifying in-canopy first-order closure approximation with a constant mixing-length (yielding an exponentially decaying eddy diffusivity for scalars; Bonan et al., 2018, their Eq. 22) cannot reproduce this canopy-induced non-local mixing. While higher-order mixing schemes (e.g., Falk et al., 2014; Xu et al., 2014) can reproduce non-local in-canopy mixing, these higher-order schemes introduce numerous tunable parameters, can become numerically unstable, and are not yet able to account for the additional turbulence canopies generate (Raupach et al., 1996; Finnigan et al., 2009). The first-order closure allows for a numerically robust and efficient solution using a system of linear equations to solve for air temperature, water vapor concentration, and leaf temperature at each height (see Bonan et al., 2018, their Eqs. 16–17). The numerical method facilitates coupling in a global climate model, but at the cost of model accuracy.

CLM5/6 uses an ad-hoc parameterization of under-canopy turbulence to calculate the flux of sensible heat in the canopy. The under-canopy aerodynamic conductance between the soil and canopy air is parameterized as the product of a transfer coefficient ($C_s = 0.004$ for dense vegetation) multiplied by the wind speed in the canopy (U_{af}; see Lawrence et al., 2018, their Eq. 2.5.116), which originates from Dickinson et al. (1993, see their Eq. 65). The conceptual framework is unchanged over 30+ years of model development, but various versions of CLM have changed C_s and wind speed as needed for the particular model configuration: C_s modified for sparse canopies (CLM3); C_s adjusted for under-canopy stability (CLM4); and the under-canopy stability adjustment removed (CLM5). The under-canopy turbulence has been updated again with the implementation of biomass heat storage (Swenson et al., 2019; Meier et al., 2019) as part of the revised CLM6. That implementation introduces an under-canopy wind speed defined as $U_{uc} = 0.03u_{\mathrm{ref}}/u_* \le 0.4$, where u_{ref} is the atmosphere forcing height wind speed. U_{af} is the wind speed on foliage used for leaf boundary layer conductance (as in CLM5), and U_{uc} replaces U_{af} when calculating the under-canopy conductance. In this way, the biomass heat storage implementation in CLM6 changes sensible and latent heat fluxes from the soil in a way that is unrelated to the storage of heat in biomass.

In CLM-ml v2, each layer in the canopy has an air temperature at an associated height above ground. In contrast, the temperature of the canopy air is vaguely referenced to height in CLM5/6. The canopy air temperature in CLM5/6 is defined at a height equal to the displacement height plus the roughness length ($d + z_0$; the apparent sink for momentum). In CLM5, the temperature is diagnosed as a weighted mean of the above-canopy atmospheric forcing temperature, vegetation temperature, and ground temperature (see Lawrence et al., 2018, their Eq. 2.5.93). The formulation originates with Dickinson (1984), who used the same equation (see his Eq. 19). CLM6, with the addition of biomass heat storage to the canopy energy balance, adds an extra term for stem temperature (Swenson et al., 2019). The 2-m air temperature in CLM5/6 is taken to be 2 m above $d+z_0$ (see Lawrence et al., 2018, their Eq. 2.5.58) and is obtained from Monin–Obukhov Similarity Theory without consideration for roughness-sublayer processes (interpolating between the canopy air and atmospheric forcing temperatures). In a tall forest canopy, the height of the 2-m air temperature is therefore somewhere in the upper canopy.

Calculation of surface fluxes with strongly stable conditions has been a challenge in CLM5 (Burns et al., 2018). The universal similarity functions ϕ_m and ϕ_c attain large values with increasingly stable conditions, which results in excessively cold canopies at night. The solution in CLM5 is to restrict $\zeta = (z - d)/L \le 0.5$ (Table 1). The inclusion of biomass heat storage limits nighttime cooling and alleviates the need for the ζ restriction (Swenson et al., 2019), and CLM6 lessens the restriction to $\zeta \le 2$. Alternatively, Burns et al. (2018) recommended using Handorf et al.'s (1999) parameterization which limits the value of the universal functions in strongly stable conditions and eliminates the need for a cap on ζ. CLM-ml v2 likewise restricts L from becoming too stable. Easing the restriction on L cools nighttime temperatures within and above the canopy and increases biases compared with the observations (Fig. S.19). In contrast with the arbitrariness of the ζ restriction in CLM5/6, the restriction in CLM-ml v2 instead arises through the roughness sublayer theory's bounds of applicability based on L_c/L (Harman and Finnigan, 2007, 2008).

CLM5/6 relies on many ad-hoc fixers in calculating canopy fluxes so as to prevent oscillation in flux predictions between model timesteps (Table 1). CLM-ml v2, with its 5-min timestep, fourth-order Runge–Kutta method, and temporal interpolation of the meteorological forcing, eliminates the need for many of these fixers (Figs. 15, S.12). Without temporally interpolating the meteorological forcing, the fourth-order Runge–Kutta smooths the simulated fluxes except during the initial 5-min interval in each 30-min period. The adjustment on the first 5-min step relates to canopy heat storage. Without interpolation, the forcing height air temperature is updated every 30-min. The change in temperature occurs at the first 5-min step, and the forcing temperature is constant over the next five 5-min substeps. The canopy air adjusts rapidly to the forcing perturbation, which produces a large change in air temperature (and heat storage) over the first timestep; thereafter change in heat storage is minimal. Temporal interpolation of the forcing data distributes the change in forcing temperature over all six 5-min intervals within the 30-min period.

Heat storage in the canopy air and plant biomass is not commonly calculated at flux tower sites. CLM-ml v2 includes storage of heat in the leaves and the canopy air, but not in wood. The heat storage in the air compares favorably with the heat storage derived from the observations (Table 3, Fig. 12). Garai et al. (2010) estimated biomass heat storage at the walnut orchard and found that storage in the leaves is less than ± 1 W m^{-2}, comparable to the model, and storage in wood varies from –6 to 12 W m^{-2} depending on time of day.

In the roughness sublayer theory, roughness length (z_0) is not an imposed model parameter and instead is flow dependent based upon an observable canopy-imposed parameter (e.g., a canopy-element drag coefficient). The displacement height (d) likewise emerges from the roughness sublayer theory and depends on flow. At CHATS with a 10-m canopy, d varies by up to 2 m depending on time of day (Fig. 11). In contrast, CLM5/6 treats z_0 and d as canopy structural parameters rather than parameters dependent on the turbulent flow, which leads to ad-hoc application throughout the model. For example, the atmospheric forcing height when CLM5/6 is coupled to its host atmosphere model is relative to $d + z_0$ (i.e., the forcing height is the height above $d + z_0$).

4.2. Soil measurements

Additional soil moisture and temperature measurements with depth would have been helpful to constrain the model. We use the observed soil moisture (5-cm depth) for the top three model soil layers (to a depth of 9 cm). λE decreases and H increases as the observed soil moisture is applied to deeper soil layers, but the precise depth is not too important in the top 20 cm of soil (Fig. S.18). More fundamentally, our

modeling framework, by treating soil moisture as a boundary condition, neglects the long term coupling between evapotranspiration and soil moisture. This is reasonable for the walnut orchard, where the soil is relatively moist during May (Fig. 2), or for simulations spanning a few weeks as in Bonan et al. (2018, 2021). Applications of the model at other locations and for longer time periods (e.g., a full growing season) may necessitate coupling with CLM's soil hydrology.

The model has a large daytime bias in soil heat flux (Table 3), but the single-point soil heat flux measurements likely are not representative of the larger tower footprint. More soil measurements sampling the broader and spatially heterogeneous tower footprint would have been helpful.

4.3. Parameter estimation

Stomatal conductance is critical to obtaining simulated fluxes that correspond with the CHATS data, and leaf gas exchange measurements of photosynthesis and stomatal conductance are essential for parameter estimation. We use $V_{\mathrm{cmax25}} = 125$ μmol m^{-2} s^{-1} and $\iota = 375$ μmol $\mathrm{CO_2}$ mol^{-1} $\mathrm{H_2O}$, estimated from leaf measurements for *Juglans regia* 'Chandler'. These values replicate the high stomatal conductance seen in the observations (Fig. 6e), and they also reduce biases in H and λE (Figs. S.13, S.14). Other values of V_{cmax25} and ι result in fluxes that are inconsistent with the observations.

Plant hydraulics provides a critical control of stomatal conductance, and the simulated fluxes are very sensitive to the specified stomatal response to water stress. $\psi_{50} = -1.6$ MPa and $\alpha = 40$ give abrupt stomatal closure at leaf water potential between −1.5 and −1.8 MPa (Fig. 7) and provide a reasonable correspondence with observed above-canopy H and λE (Fig. 16). In contrast, the values $\psi_{50} = -0.45$ MPa and $\alpha = 2.60$ obtained from the Rosati et al. (2006) leaf gas exchange data cause stomata to close at high leaf water potential with the result that λE is underestimated and H is overestimated. Moreover, the simulated leaf water potential does not attain values less than −1 MPa, as commonly found in studies of walnut (Tyree et al., 1993; McElrone et al., 2010; Sun et al., 2011; Jerszurki et al., 2017; Calvo et al., 2023). Stem hydraulic conductance (k_p) additionally affects the fluxes, and the high conductance observed in walnut (Table 2) improves model performance compared with lower values (Fig. S.15).

Plant physiological parameters do not just affect leaf source fluxes; through the fluxes they influence the state of the canopy air space. Stomatal conductance, as determined by V_{cmax25} and ι, and stomatal closure with water stress (ψ_{50} and α) influence air temperature in the canopy, with warmer daytime temperatures at lower V_{cmax25} (Fig. S.13), higher ι (Fig. S.14), and with stomatal closure at high leaf water potential (Fig. 16).

The simulations are improved with the optical properties for leaf angle distribution, leaf reflectance, leaf transmittance, and stem reflectance obtained from Majasalmi and Bright (2019). CLM-ml v1 uses the optical properties of CLM5 (Lawrence et al., 2018). The biggest changes compared to CLM-ml v1 are that leaf angle distribution is more horizontal; leaf transmittance increases by 0.18 in the near-infrared waveband; and stem reflectance increases by 0.05 (visible) and 0.10 (near-infrared) (Table 2). As a result, the canopy absorbs less solar radiation, and biases in R_{net}, H, and λE decrease (Fig. S.17). There is little difference between the optical properties for walnut and the values proposed by Majasalmi and Bright (2019) for temperate broadleaf deciduous tree.

Above-canopy fluxes of R_{net}, H, and λE are not sensitive to the canopy-element drag coefficient (Fig. 17). Varying c_d from 0.15 to 0.4 has negligible effect on these fluxes. However, c_d critically affects u_* and air temperature. Our estimate of c_d obtained from observed in-canopy momentum flux profiles (Fig. 5b) is similar to the value of $c_d = 0.25$ used in previous CLM-ml simulations (Bonan et al., 2018, 2021) and that value may be a general value in the absence of observed momentum flux profiles. Other canopy-specific parameters are β_{N}, a_1, a_2, and a_3, used in Eq. (2) to calculate β. The values for the 10-m walnut orchard are similar to those estimated by Harman (2012) for Tumbarumba (a 40-m tall eucalyptus forest), and the similarity in the functional form of Eq. (2) suggests a broad generality across a diverse range of canopy structures (Fig. 3).

4.4. Coupling component models

The roughness sublayer theory as currently implemented in CLM-ml v2 is not without deficiencies (especially in strongly stable conditions), but it provides a self-consistent theory that unifies above and within canopy processes. Other modeling efforts are recognizing the need to account for vertically-resolved plant canopies, but end up coupling component models that do not necessarily have consistent physics. For example, Hung et al. (2024) developed a parameterization of canopy wind speed to calculate wildfire spread in numerical weather prediction models, but the implementation is inconsistent with the turbulence parameterization used to couple the land surface with the boundary layer. As another example, the FATES vegetation demography model uses the vertical profile of light to calculate photosynthesis and stomatal conductance in a height-structured canopy, but collapses the vertically-resolved stomatal conductance to an integrated canopy conductance to couple with CLM's big-leaf canopy (Koven et al., 2020). Early in the development of the first generation of land surface models it was recognized that "the physiological state of a plant community substantially influences the microclimate within it; in turn, the microclimate influences the physiological state, so that neither is independent of the other" (Finnigan and Raupach, 1987). The coupled system, with many biophysical interdependencies, needs to be remembered when developing new components for land surface models.

The replacement of CLM's existing surface flux code with CLM-ml is conceptually straightforward, but is difficult in practice. Several decades of model development has produced code that, while internally consistent and advanced in its capabilities, is not robust beyond CLM's big-leaf canopy representation. The software engineering of CLM, in which canopy processes are spread across multiple routines, require model-specific interfaces, and perform calculations in addition to their stated purpose, precludes simple replacement of single-layer (big-leaf) code with equivalent multilayer code. Additional science capabilities in CLM such as water isotopes, ozone stress, dry deposition, and biogenic volatile organic compound emissions also use the big-leaf canopy implementation. When CLM's dynamic vegetation is enabled, canopy height, leaf area, and stem area change over time, which further complicates the interface with the multilayer canopy.

The implementation of a multilayer canopy in CLM also exposes inconsistencies in the coupling between the land and atmosphere. In version 7 of the Community Atmosphere Model (CAM; Simpson et al., 2025, CLM's host model), the lowest level of the atmosphere is approximately 17 m, which is lower than the height of many tall forests. The solution in previous model versions is to interpret the atmospheric height as above $d + z_0$. By simulating the air space below CAM's lowest level, the multilayer canopy extends the boundary layer to the ground. Approaches that directly extend CAM's boundary layer parameterization (CLUBB; Golaz et al., 2002; Larson et al., 2002) to the ground with a multilayer canopy may provide a more unified coupling between land and atmosphere — assuming pathways exist to bring roughness sublayer physics into CLUBB's higher-order closure framework.

5. Conclusions

Multilayer canopies extend the science capabilities of land surface models. Multilayer canopies enable simulation of the surface air (temperature, humidity, wind speed) between the lowest level of an atmospheric model and the ground, where terrestrial life occurs. This is the air that is neglected in both atmosphere and land models. In doing

so, multilayer canopies reframe the land surface from a flux boundary condition with the atmosphere to a focal point of climate prediction. The CLM-ml v2 multilayer canopy has noticeable deficiencies (especially in strongly stable regimes), but it is more correct (i.e., physically based) in the sense of Raupach and Finnigan (1988), and it reduces much of the ad-hoc parameterization in CLM5/6. Multilayer canopy models additionally enable new science. The models specifically distinguish forest overstory from understory environments, and therefore can inform biological conservation. They allow for direct comparison with leaf measurements (photosynthesis, stomatal conductance, leaf temperature, leaf water potential) at various heights in the canopy, and they provide a path to simulate chemistry in plant canopies (e.g., dry deposition, biogenic volatile organic compounds). For example, a multilayer canopy improves model estimates of ozone deposition (Vermeuel et al., 2024).

To realize the science potential of multilayer canopies, high quality, comprehensive datasets are needed to test model assumptions and guide model development. The CHATS dataset provides one such set of observations. Measurements of air temperature, water vapor, and wind speed within and above the canopy, as well as vertical profiles of net radiation, sensible heat, latent heat, and momentum, critically inform model development. The CLM-ml v2 multilayer model captures many important aspects of the canopy of the walnut orchard, but better understanding of the strongly stable regime, when the upper canopy is decoupled from the lower canopy, is critically needed and should be a focus of future observational programs and modeling. Measurements of soil heat flux, soil temperature, and soil moisture are needed to better constrain fluxes at the ground. Measurements of leaf gas exchange (photosynthesis, stomatal conductance) and the leaf environment (leaf water potential, leaf temperature) concomitant with the flux/scalar profile measurements would aid in reducing uncertainty in the model–data comparisons. Observational programs must expand beyond measuring single-point above-canopy surface fluxes to provide a comprehensive understanding of the microclimate of plant canopies.

CRediT authorship contribution statement

Gordon B. Bonan: Writing – original draft, Methodology, Formal analysis, Conceptualization. **Sean P. Burns:** Writing – review & editing, Visualization, Methodology, Formal analysis, Data curation, Conceptualization. **Edward G. Patton:** Writing – review & editing, Methodology, Formal analysis, Conceptualization.

Declaration of competing interest

The authors declare that they have no known competing financial interests or personal relationships that could have appeared to influence the work reported in this paper.

Acknowledgments

This material is based upon work supported by the NSF National Center for Atmospheric Research (NCAR), United States, which is a major facility sponsored by the National Science Foundation (NSF), United States under Cooperative Agreement No. 1852977. The authors also acknowledge fruitful discussions regarding this work with John Finnigan (CSIRO) and Martin Béland (Laval University).

Appendix A. Measurement post-processing

A.1. Flux calculation

Turbulent fluxes of sensible heat (H) and latent heat (λE) are calculated from the covariance between vertical wind (w) and air temperature (T) or water vapor density (ρ_v) fluctuations following:

$$H = \rho\, c_p\, \overline{w'T'} \tag{A.1}$$

$$\lambda E = \lambda\, \overline{w'\rho_v'} \tag{A.2}$$

where ρ is the mean air density (kg m^{-3}), c_p is the mean specific heat of moist air at constant pressure (J kg^{-1} K^{-1}), and λ is the mean latent heat of vaporization of water (J kg^{-1}). Note that $\rho = \rho_a + \rho_v$ and $c_p = (\rho_a c_{p_a} + \rho_v c_{p_v})/\rho$, where the subscripts a and v refer to dry air and water vapor, respectively. Unless otherwise noted, means and fluctuations are calculated over a 30-min period and overbars are only shown on the covariance terms.

A.1.1. Covariances

As their standard product, NSF NCAR EOL provides 5-min means and covariances (Horst, 2020). The 5-min statistics are used to calculate the 30-min turbulent fluxes where the low-frequency information needs to be taken into account (ISFS, 2025). For example, to calculate the 30-min covariance between the sonic anemometer temperature (T_s) and vertical wind (w), the following is used:

$$\overline{w'T_s'} = \frac{1}{6}\sum_{j=1}^{6}(\overline{w'T_s'}^{\,j} + \overline{w}^{j}\overline{T_s}^{\,j}) - \frac{1}{6}\sum_{j=1}^{6}\overline{w}^{j}\,\frac{1}{6}\sum_{j=1}^{6}\overline{T_s}^{\,j} \tag{A.3}$$

where $\overline{w'T_s'}$ is the 30-min covariance, and all the terms on the right-side of Eq. (A.3) are 5-min statistics summed over six 5-min periods. Similar expressions are used for $\overline{w'v'}$, $\overline{w'\rho_v'}$, etc. The effect of using Eq. (A.3) compared to taking a simple average is to increase H by around about 4%–5% (the impact is primarily during the daytime when larger-scale eddies are contributing to the flux, which is not captured by a 5-minute averaging window).

A.1.2. Additional flux terms and corrections

Additional terms are required to the calculate (H) and (λE) from the 30-min covariances. Because temperature and humidity both influence the speed of sound, temperature fluctuations measured by sonic anemometry such as the CSAT3 deployed during CHATS (Campbell Scientific Inc., 2017) are more similar to virtual temperature fluctuations than true air temperature fluctuations. Therefore, we use the Schotanus correction (Schotanus et al., 1983; Foken et al., 2012) to convert sonic temperature into air temperature (i.e., to remove water vapor's influence). Sensible heat flux is therefore calculated from sonic anemometer temperature (T_s) using:

$$H = \rho\, c_p \left[\overline{w'T_s'} - 0.51\, T\, \overline{w'q'}\right] \tag{A.4}$$

where q is specific humidity measured with a nearby fast-response humidity sensor (Campbell Scientific Inc., 2021). At CHATS, there were 13 levels of sonic anemometry on the tower and only 6 levels of krypton hygrometers. Therefore, $\overline{w'q'}$ comes from the krypton nearest to the sonic anemometer to calculate the Schotanus term. The krypton at the 14-m level was missing a lot of data; therefore, the 23-m krypton is used for the Schotanus corrections of any sonic anemometers at 14 m and higher. On average, the Schotanus correction decreases H by around 5%.

Krypton hygrometers use a krypton lamp and Lambert–Beer's law of absorption to measure water vapor fluctuations in the atmosphere (van Dijk et al., 2003; Foken and Falke, 2012; Campbell Scientific Inc., 2021). The instrument operates at two spectral bands (wavelengths of 116.49 nm and 123.58 nm), and the 116.49 nm wavelength band is

attenuated by both water vapor and oxygen. Therefore, a correction for the absorption due to the oxygen is required. For the oxygen-correction, we follow Oncley et al. (2007):

$$\overline{w'\rho_v'} = \overline{w'(\rho_v')_{kr}} + C_{ko}\frac{\rho_a}{T}\overline{w'T'} \tag{A.5}$$

where $(\rho_v')_{kr}$ is the water vapor density output from the krypton hygrometer and the second term is the oxygen correction. C_{ko} is the correction factor for the oxygen absorption, which is calculated via:

$$C_{ko} = (K_o/K_w)(C_o\frac{M_o}{M_a}) = 0.23(K_o/K_w) \tag{A.6}$$

where $C_o = 0.21$ is the fraction of oxygen in the atmosphere, and the molecular weights of oxygen and dry air are $M_o = 32$ and $M_a = 28.97$ g mol^{-1}, respectively. K_o and K_w are the krypton hygrometer extinction coefficients for oxygen and water vapor. K_o depends on the path length of the krypton hygrometer, and we use $K_o = -0.0034\,\mathrm{m^3\ g^{-1}\ cm^{-1}}$ as recommended in the "Krypton Hygrometers" section of the CHATS data report (CHATS project webpage, 2007). The report also provides the K_w value for each individual krypton used in the data processing. For CHATS, the K_w values range between −0.143 and $-0.152\,\mathrm{m^3\ g^{-1}\ cm^{-1}}$. The oxygen-correction for λE is small (less than 0.5%).

Latent heat fluxes (λE) include the Webb–Pearman–Leuning (WPL) term (Webb et al., 1980; Fuehrer and Friehe, 2002) which is:

$$\lambda E = \lambda\left(1+\mu\frac{\rho_v}{\rho_a}\right)\left[\overline{w'\rho_v'} + \frac{\rho_v}{T}\overline{w'T'}\right] \tag{A.7}$$

where $\mu = M_a/M_v = 28.97/18.02 = 1.608$ is the ratio of the molecular weight of dry air (M_a) to that of water (M_v), $\overline{w'\rho_v'}$ is from Eq. (A.5), and $\overline{w'T'}$ is from the two terms within the brackets in Eq. (A.4). Including the WPL term increases λE by around 1%.

A.2. Mean air properties

The moist air density (ρ), specific heat of moist air at constant pressure (c_p), and latent heat of vaporization (λ) vary with air temperature, pressure, and humidity. These air properties are typically evaluated at the mean air temperature and pressure at the sensor locations; λ, however, should be evaluated at the surface temperature where evapotranspiration occurs. The moist air density is:

$$\rho = \rho_a + \rho_v = \frac{p-e}{R_d T} + \frac{e}{R_v T} \tag{A.8}$$

where p is pressure, e is the partial pressure of water vapor, R_d is the gas constant for dry air ($R_d = 287\,\mathrm{J\,kg^{-1}\,K^{-1}}$), and R_v is the gas constant for water vapor ($R_v = 461.5\,\mathrm{J\,kg^{-1}\,K^{-1}}$). In this equation, e is obtained from relative humidity and the saturated vapor pressure (e_s). For our study, the temperature-dependence of e_s is calculated using the Goff–Gratch formulation (Goff and Gratch, 1946).

The specific heat of moist air at constant pressure is:

$$c_p = \frac{\rho_a}{\rho}c_{p_a} + \frac{\rho_v}{\rho}c_{p_v} \tag{A.9}$$

which can be equivalently written:

$$c_p = c_{p_a}\left[1+\frac{\rho_v}{\rho}\left(\frac{c_{p_v}-c_{p_a}}{c_{p_a}}\right)\right] \tag{A.10}$$

In this equation, the specific heat of dry air (c_{p_a}) has a weak temperature dependence (Garratt, 1992):

$$c_{p_a} = 1005 + \frac{(T-250)^2}{3364}, \tag{A.11}$$

where the value of 1005 J kg^{-1} K^{-1} is the specific heat of dry air at $T = 250$ K. We use $c_{p_v} = 1850$ J kg^{-1} K^{-1} for the specific heat of water vapor. Because $(c_{p_v} - c_{p_a})/c_{p_a} \approx 0.84$, c_p simplifies to:

$$c_p \approx c_{p_a}\left(1+0.84\frac{\rho_v}{\rho}\right) \tag{A.12}$$

The temperature-dependence of the latent heat of vaporization (Bolton, 1980; Foken, 2017) is:

$$\lambda = (2.501 - 0.00237\,T)\times 10^6 \tag{A.13}$$

where T is in °C. This empirical relationship agrees quite well with WMO-tabulated values of λ from Letestu (1966). To estimate λ at the evaporating surfaces, T was calculated from the median of the four lowest T/RH sensors on the vertical CHATS tower (all are within the subcanopy).

A.3. Air heat storage

The heat stored in the air space between the ground and the 23-m measurement height (S) is calculated with (Turnipseed et al., 2002; Leuning et al., 2012):

$$S = \rho\, c_p \int_0^{23\,\mathrm{m}} \frac{dT}{dt}\,dz + \rho\,\lambda\int_0^{23\,\mathrm{m}}\frac{dq}{dt}\,dz \tag{A.14}$$

where air temperature (T) and specific humidity (q) are from the vertical profile of T/RH sensors on the tower, and air density (ρ), specific heat (c_p), and latent heat of vaporization (λ) calculations are described above in Appendix A.2. In Eq. (A.14), the first term is the air sensible heat storage and the second term is the latent heat storage.

A.4. Radiation measurements

Above-canopy radiation was measured at 16 m with a Kipp and Zonen 4-component radiometer (CM21 pyranometers and CG4 pyrgeometers). At 2 m in the subcanopy, EOL-modified (e.g., Delany and Semmer, 1998; Burns et al., 2003) pairs of Eppley model PSP (for shortwave) and model PIR (for longwave) sensors were deployed.

To calculate longwave irradiance (R_{LW}) from an Eppley PIR, we follow ISFS (2025) by using:

$$R_{\mathrm{LW}} = R_{pile} + \sigma T_{\mathrm{c}}^4 - B\sigma(T_{\mathrm{d}}^4 - T_{\mathrm{c}}^4) + f\,R_{\mathrm{SW}} \tag{A.15}$$

where R_{pile} is the thermopile output, σ is the Stefan–Boltzmann constant (5.67×10^{-8} W m^{-2} K^{-4}), T_{c} is the case temperature, T_{d} is the dome temperature, B is the ratio of the dome emissivity to the transmissivity (sometimes called the "dome factor"), f is a correction factor, and R_{SW} is shortwave radiation. Though analytic expressions exist for B, they are usually determined by lab calibration. As described in the ISFS (2025), B and f are both sensor-specific values determined by shading tests in clear-sky conditions. Typical values for B are from 1.8–4.0 while for f they are from 0.5–1.9%. For CHATS, $B = 4$ was used and the $f\,R_{\mathrm{SW}}$ term was neglected. Additional discussion of Eq. (A.15) can be found in Burns et al. (2003) and in the ISFS (2025).

Appendix B. Supplementary data

Supplementary material related to this article can be found online at https://doi.org/10.1016/j.agrformet.2025.110960.

Data availability

The CLM-ml v2 source code and datasets to run the CHATS simulations are available at github.com/gbonan. The 30-minute observation dataset created and used for model evaluation in this study is available at doi.org/10.5281/zenodo.17426258.

References

Abramowitz, G., Ukkola, A., Hobeichi, S., Cranko Page, J., Lipson, M., De Kauwe, M.G., Green, S., Brenner, C., Frame, J., Nearing, G., Clark, M., Best, M., Anthoni, P., Arduini, G., Boussetta, S., Caldararu, S., Cho, K., Cuntz, M., Fairbairn, D., Ferguson, C.R., Kim, H., Kim, Y., Knauer, J., Lawrence, D., Luo, X., Malyshev, S., Nitta, T., Ogee, J., Oleson, K., Ottlé, C., Peylin, P., de Rosnay, P., Rumbold, H., Su, B., Vuichard, N., Walker, A.P., Wang-Faivre, X., Wang, Y., Zeng, Y., 2024. On the predictability of turbulent fluxes from land: PLUMBER2 MIP experimental description and preliminary results. Biogeosci. 21, 5517–5538. http://dx.doi.org/10.5194/bg-21-5517-2024.

Best, M.J., Abramowitz, G., Johnson, H.R., Pitman, A.J., Balsamo, G., Boone, A., Cuntz, M., Decharme, B., Dirmeyer, P.A., Dong, J., Ek, M., Guo, Z., Haverd, V., van den Hurk, G.S., Pak, B., Peters-Lidard, C., Santanello, J.A., Stevens, L., Vuichard, N., 2015. The plumbing of land surface models: Benchmarking model performance. J. Hydrometeorol. 16, 1425–1442. http://dx.doi.org/10.1175/JHM-D-14-0158.1.

Bolton, D., 1980. The computation of equivalent potential temperature. Mon. Weather Rev. 108, 1046–1053. http://dx.doi.org/10.1175/1520-0493(1980)108<1046:TCOEPT>2.0.CO;2.

Bonan, G.B., Patton, E.G., Finnigan, J.J., Baldocchi, D.D., Harman, I.N., 2021. Moving beyond the incorrect but useful paradigm: reevaluating big-leaf and multilayer plant canopies to model biosphere-atmosphere fluxes – a review. Agric. For. Meteorol. 306, 1–23. http://dx.doi.org/10.1016/j.agrformet.2021.108435.

Bonan, G.B., Patton, E.G., Harman, I.N., Oleson, K.W., Finnigan, J.J., Lu, Y., Burakowski, E.A., 2018. Modeling canopy-induced turbulence in the earth system: a unified parameterization of turbulent exchange within plant canopies and the roughness sublayer (CLM-ml v0). Geosci. Model. Dev. 11, 1467–1496. http://dx.doi.org/10.5194/gmd-11-1467-2018.

Bonan, G.B., Williams, M., Fisher, R.A., Oleson, K.W., 2014. Modeling stomatal conductance in the earth system: linking leaf water-use efficiency and water transport along the soil–plant–atmosphere continuum. Geosci. Model. Dev. 7, 2193–2222. http://dx.doi.org/10.5194/gmd-7-2193-2014.

Brown, J.S., Shapkalijevski, M.M., Krol, M.C., Karl, T., Ouwersloot, H.G., Moene, A.F., Patton, E.G., De Arellano, J.V.G., 2020. Ozone exchange within and above an irrigated Californian orchard. Tellus B 72, 1–17. http://dx.doi.org/10.1080/16000889.2020.1723346.

Brunet, Y., Finnigan, J.J., Raupach, M.R., 1994. A wind-tunnel study of air-flow in waving wheat: Single-point velocity statistics. Bound.-Layer Meteorol. 70, 95–132. http://dx.doi.org/10.1007/BF00712525.

Brutsaert, W., 1982. Evaporation Into the Atmosphere: Theory, History, and Applications. Kluwer, Dordrecht, p. 299. http://dx.doi.org/10.1007/978-94-017-1497-6.

Burns, S.P., Sun, J., Delany, A.C., Semmer, S.R., Oncley, S.P., Horst, T.W., 2003. A field intercomparison technique to improve the relative accuracy of longwave radiation measurements and an evaluation of CASES-99 pyrgeometer data quality. J. Atmos. Ocean. Technol. 20, 348–361. http://dx.doi.org/10.1175/1520-0426(2003)020<0348:AFITTI>2.0.CO;2.

Burns, S.P., Sun, J., Lenschow, D.H., Oncley, S.P., Stephens, B.B., Yi, C., Anderson, D.E., Hu, J., Monson, R.K., 2011. Atmospheric stability effects on wind fields and scalar mixing within and just above a subalpine forest in sloping terrain. Bound.-Layer Meteorol. 138, 231–262. http://dx.doi.org/10.1007/s10546-010-9560-6.

Burns, S.P., Swenson, S.C., Wieder, W.R., Lawrence, D.M., Bonan, G.B., Knowles, J.F., Blanken, P.D., 2018. A comparison of the diel cycle of modeled and measured latent heat flux during the warm season in a colorado subalpine forest. J. Adv. Model. Earth Syst. 10, 617–651. http://dx.doi.org/10.1002/2017MS001248.

Businger, J.A., 1973. Turbulent transfer in the atmospheric surface layer. In: Haugen, D.A. (Ed.), Workshop on Micrometeorology. Amer. Meteorol. Soc., Boston, MA, pp. 67–100.

Businger, J.A., Wyngaard, J.C., Izumi, Y., Bradley, E.F., 1971. Flux-profile relationships in the atmospheric surface layer. J. Atmos. Sci. 28, 181–189. http://dx.doi.org/10.1175/1520-0469(1971)028<0181:FPRITA>2.0.CO;2.

Calvo, F.E., Silvente, S.T., Trentacoste, E.R., 2023. A mini review of the impacts of deficit irrigation strategies for walnut (*Juglans regia* L.) production in semiarid conditions. Irrig. Sci. 41, 501–509. http://dx.doi.org/10.1007/s00271-022-00815-w.

Campbell Scientific Inc., 2017. Instruction manual: CSAT3 three dimensional sonic anemometer, revision 4/17. https://s.campbellsci.com/documents/us/manuals/csat3.pdf. (Accessed 11 July 2025).

Campbell Scientific Inc., 2021. Product manual: KH20 krypton hygrometer, revision 04/2021. https://s.campbellsci.com/documents/us/manuals/kh20.pdf. (Accessed 11 July 2025).

CHATS project webpage, 2007. https://www.eol.ucar.edu/field_projects/chats. (Accessed 11 July 2025).

Chen, Y., Ryder, J., Bastrikov, V., McGrath, M.J., Naudts, K., Otto, J., Ottlé, C., Peylin, P., Polcher, J., Valade, A., Black, A., Elbers, J.A., Moors, E., Foken, T., van Gorsel, E., Haverd, V., Heinesch, B., Tiedemann, F., Knohl, A., Launiainen, S., Loustau, D., Ogée, J., Vessala, T., Luyssaert, S., 2016. Evaluating the performance of land surface model ORCHIDEE-CAN v1.0 on water and energy flux estimation with a single- and multi-layer energy budget scheme. Geosci. Model. Dev. 9, 2951–2972. http://dx.doi.org/10.5194/gmd-9-2951-2016.

Chianucci, F., Pisek, J., Raabe, K., Marchino, L., Ferrara, C., Corona, P., 2018. A dataset of leaf inclination angles for temperate and boreal broadleaf woody species. Ann. For. Sci. 75, 50. http://dx.doi.org/10.1007/s13595-018-0730-x.

Cionco, R.M., 1965. A mathematical model for air flow in a vegetative canopy. J. Appl. Meteorol. Clim. 4, 517–522. http://dx.doi.org/10.1175/1520-0450(1965)004<0517:AMMFAF>2.0.CO;2.

Cionco, R.M., 1978. Analysis of canopy index values for various canopy densities. Bound.-Layer Meteorol. 15, 81–93. http://dx.doi.org/10.1007/BF00165507.

Cochard, H., Coll, L., Le Roux, X., Améglio, T., 2002. Unraveling the effects of plant hydraulics on stomatal closure during water stress in walnut. Plant Physiol. 128, 282–290. http://dx.doi.org/10.1104/pp.010400.

Cowan, I.R., 1968. Mass, heat and momentum exchange between stands of plants and their atmospheric environment. Q. J. R. Meteorol. Soc. 94, 523–544. http://dx.doi.org/10.1002/qj.49709440208.

Danabasoglu, G., Lamarque, J.F., Bacmeister, J., Bailey, D.A., DuVivier, A.K., Edwards, J., Emmons, L.K., Fasullo, J., Garcia, R., Gettelman, A., Hannay, C., Holland, .M.M., Large, W.G., Lauritzen, P.H., Lawrence, D.M., Lenaerts, J.T.M., Lindsay, K., Lipscomb, W.H., Mills, M.J., Neale, R., Oleson, K.W., Otto-Bliesner, B., Phillips, A.S., Sacks, W., Tilmes, S., Kampenhout, L.van., Vertenstein, M., Bertini, A., Dennis, J., Deser, C., Fischer, C., Fox-Kemper, B., Kay, J.E., Kinnison, D., Kushner, P.J., Larson, V.E., Long, M.C., Mickelson, S., Moore, J.K., Nienhouse, E., Polvani, L., Rasch, P.J., Strand, .W.G., 2020. The community earth system model version 2 (CESM2). J. Adv. Model. Earth Syst. 12, e2019MS001916. http://dx.doi.org/10.1029/2019MS001916.

De Frenne, P., Lenoir, J., Luoto, M., Scheffers, B.R., Zellweger, F., Aalto, J., Ashcroft, M.B., Christiansen, D.M., Decocq, G., De Pauw, K., Govaert, S., Greiser, C., Gril, E., Hampe, A., Jucker, T., Klinges, D.H., Koelemeijer, I.A., Lembrechts, J.J., Marrec, R., Meeussen, C., Ogée, J., Tyystjärvi, V., Vangansbeke, P., Hylander, K., 2021. Forest microclimates and climate change: Importance, drivers and future research agenda. Glob. Chang. Biol. 27, 2279–2297. http://dx.doi.org/10.1111/gcb.15569.

De Frenne, P., Zellweger, F., Rodríguez-Sánchez, F., Scheffers, B.R., Hylander, K., Luoto, M., Vellend, M., Verheyen, K., Lenoir, J., 2019. Global buffering of temperatures under forest canopies. Nat. Ecol. Evol. 3, 744–749. http://dx.doi.org/10.1038/s41559-019-0842-1.

De Lombaerde, P., Lenoir, J., Van Meerbeek, J., Rodríguez-Sánchez, F., Luoto, M., Scheffers, B., Haesen, S., Aalto, J., Christiansen, D.M., De Pauw, L., Govaert, S., Greiser, C., Hampe, A., Hylander, K., Klinges, D., Koelemeijer, I., Meeussen, C., Ogée, J., Sanczuk, P., Vanneste, T., Zellweger, F., Baeten, L., De Frenne, P., 2022. Maintaining forest cover to enhance temperature buffering under future climate change. Sci. Total Env. 810, 151338. http://dx.doi.org/10.1016/j.scitotenv.2021.151338.

Deardorff, J.W., 1978. Efficient prediction of ground surface temperature and moisture, with inclusion of a layer of vegetation. J. Geophys. Res. 83C, 1889–1903. http://dx.doi.org/10.1029/JC083iC04p01889.

Delany, A.C., Semmer, S.R., 1998. An integrated surface radiation measurement system. J. Atmos. Ocean. Technol. 15, 46–53. http://dx.doi.org/10.1175/1520-0426(1998)015<0046:AISRMS>2.0.CO;2.

Dickinson, R.E., 1984. Modeling evapotranspiration for three-dimensional global climate models. In: Hansen, J.E., Takahashi, T. (Eds.), Climate Processes and Climate Sensitivity. In: Geophysical Mongraphs, vol. 29, American Geophyiscal Union, Washington, D.C, pp. 58–72. http://dx.doi.org/10.1029/GM029p0058.

Dickinson, R.E., Henderson-Sellers, A., Kennedy, P.J., 1993. Biosphere–Atmosphere Transfer Scheme (BATS) Version 1e as Coupled to the NCAR Community Climate Model. Technical Report NCAR/TN-387+STR, NSF National Center for Atmospheric Research, Boulder, Colorado, http://dx.doi.org/10.5065/D67W6959.

Dickinson, R.E., Henderson-Sellers, A., Kennedy, P.J., Wilson, M.F., 1986. Biosphere–Atmosphere Transfer Scheme (BATS) for the NCAR CoMmunity Climate Model. Technical Report NCAR/TN-275+STR, NSF National Center for Atmospheric Research, Boulder, Colorado, http://dx.doi.org/10.5065/D6668B58.

Dickinson, R.E., Jäger, J., Washington, W.M., Wolski, R., 1981. Boundary Subroutine for the NCAR Global Climate Model. Technical Report NCAR/TN-173+IA, NSF National Center for Atmospheric Research, Boulder, Colorado, http://dx.doi.org/10.5065/D6CR5R9Z.

Dupont, S., Patton, E.G., 2012a. Influence of stability and seasonal canopy changes on micrometeorology within and above an orchard canopy: The CHATS experiment. Agric. For. Meteorol. 157, 11–29. http://dx.doi.org/10.1016/j.agrformet.2012.01.011.

Dupont, S., Patton, E.G., 2012b. Momentum and scalar transport within a vegetation canopy following atmospheric stability and seasonal canopy changes: the CHATS experiment. Atmos. Chem. Phys. 12, 5913–5935. http://dx.doi.org/10.5194/acp-12-5913-2012.

Falk, M., Pyles, R.D., Ustin, S.L., U, K.T.P., Xu, L., Whiting, M.L., Sanden, B.L., Brown, P.H., 2014. Evaluated crop evapotranspiration over a region of irrigated orchards with the improved ACASA–WRF model. J. Hydrometeorol. 15, 744–758. http://dx.doi.org/10.1175/JHM-D-12-0183.1.

Finnigan, J., Harman, I., Ross, A., Belcher, S., 2015. First-order turbulence closure for modelling complex canopy flows. Q. J. R. Meteorol. Soc. 141, 2907–2916. http://dx.doi.org/10.1002/qj.2577.

Finnigan, J.J., Raupach, M.R., 1987. Transfer processes in plant canopies in relation to stomatal characteristics. In: Zeiger, E., Farquhar, G.D., Cowan, I.R. (Eds.), Stomatal Function. Stanford University Press, Stanford, CA, pp. 385–429.

Finnigan, J.J., Shaw, R.H., Patton, E.G., 2009. Turbulence structure above a vegetation canopy. J. Fluid Mech. 637, 387–424. http://dx.doi.org/10.1017/S0022112009990589.

Foken, T., 2017. Micrometeorology, second ed. Springer-Verlag, Berlin, Germany, p. 362. http://dx.doi.org/10.1007/978-3-540-74666-9.

Foken, T., Falke, H., 2012. Technical note: Calibration device for the krypton hygrometer KH20. Atmos. Meas. Tech. 5, 1861–1867. http://dx.doi.org/10.5194/amt-5-1861-2012.

Foken, T., Leuning, R., Oncley, S., Mauder, M., Aubinet, M., 2012. Corrections and data quality control. In: Aubinet, M., Vesala, T., Papale, D. (Eds.), Eddy Covariance: A Practical Guide to Measurement and Data Analysis. Springer Atmospheric Sciences, Dordrecht, the Netherlands, pp. 85–131. http://dx.doi.org/10.1007/978-94-007-2351-1_4.

Fuehrer, P.L., Friehe, C.A., 2002. Flux corrections revisited. Bound.-Layer Meteorol. 102, 415–458. http://dx.doi.org/10.1023/A:1013826900579.

Galperin, B., Sukoriansky, S., Anderson, P.S., 2007. On the critical Richardson number in stably stratified turbulence. Atmos. Sci. Lett. 8, 65–69. http://dx.doi.org/10.1002/asl.153.

Garai, A., Kleissl, J., Llewellyn Smith, S.G., 2010. Estimation of biomass heat storage using thermal infrared imagery: Application to a walnut orchard. Bound.-Layer Meteorol. 137, 333–342. http://dx.doi.org/10.1007/s10546-010-9524-x.

Garratt, J.R., 1992. The Atmospheric Boundary Layer. Cambridge University Press, Cambridge, p. 316.

Goff, J.A., Gratch, S., 1946. Low-pressure properties of water from 160 to 212 °F. In: Transactions of the American Society of Heating and Ventilating Engineers, 52nd Annual Meeting of the American Society of Heating and Ventilating Engineers, New York. pp. 95–122.

Golaz, J.C., Larson, V.E., Cotton, W.R., 2002. A PDF-based model for boundary layer clouds. Part I: Method and model description. J. Atmos. Sci. 59, 3540–3551. http://dx.doi.org/10.1175/1520-0469(2002)059<3540:APBMFB>2.0.CO;2.

Goudriaan, J., 1977. Crop Micrometeorology: A Simulation Study. Center for Agricultural Publishing and Documentation, Wageningen.

Goudriaan, J., Waggoner, P., 1972. Simulating both aerial microclimate and soil temperature from observation above the foliar canopy. Neth. J. Agric. Sci. 20, 104–124. http://dx.doi.org/10.18174/njas.v20i2.17290.

Handorf, D., Foken, T., Kottmeier, C., 1999. The stable atmospheric boundary layer over an antarctic ice sheet. Bound.-Layer Meteorol. 91, 165–189. http://dx.doi.org/10.1023/A:1001889423449.

Harman, I.N., 2012. The role of roughness sublayer dynamics within surface exchange schemes. Bound.-Layer Meteorol. 142, 1–20. http://dx.doi.org/10.1007/s10546-011-9651-z.

Harman, I.N., Finnigan, J.J., 2007. A simple unified theory for flow in the canopy and roughness sublayer. Bound.-Layer Meteorol. 123, 339–363. http://dx.doi.org/10.1007/s10546-006-9145-6.

Harman, I.N., Finnigan, J.J., 2008. Scalar concentration profiles in the canopy and roughness sublayer. Bound.-Layer Meteorol. 129, 323–351. http://dx.doi.org/10.1007/s10546-008-9328-4.

Haughton, N., Abramowitz, G., Pitman, A.J., Or, D., Best, M.J., Johnson, H.R., Balsamo, G., Boone, A., Cuntz, M., Decharme, B., Dirmeyer, P.A., Dong, J., Ek, M., Guo, Z., Haverd, V., van den Hurk, B.J.J., Nearing, G.S., Pak, B., Santanello, J.A., Stevens, L.E., Vuichard, N., 2016. The plumbing of land surface models: Is poor performance a result of methodology or data quality? J. Hydrometeorol. 17, 1705–1723. http://dx.doi.org/10.1175/JHM-D-15-0171.1.

Hes, G., Vanderkelen, I., Fisher, R., Chave, J., Ogée, J., Davin, E.L., 2024. Projecting future forest microclimate using a land surface model. Env. Res. Lett. 19, 024030. http://dx.doi.org/10.1088/1748-9326/ad1f04.

Horst, T., 2020. NSF NCAR/EOL ISFS Surface Meteorology and Flux Products, 5-Min Avg, Geo-Referenced, Tilt/Flow Corrected Winds, Version 1.0 [Dataset]. NSF National Center for Atmospheric Research Earth Observing Laboratory, Boulder, Colorado, http://dx.doi.org/10.26023/HT8J-5DE0-QH0B.

Horst, T., Oncley, S., 2019. CHATS: ISFS High Rate Tower and Array Surface Meteorology and Flux Products, Version 2.0 [Dataset]. NSF National Center for Atmospheric Research Earth Observing Laboratory, Boulder, Colorado, http://dx.doi.org/10.26023/P4JW-9T0T-QG0S.

Horst, T.W., Semmer, S.R., Maclean, G., 2015. Correction of a non-orthogonal, three-component sonic anemometer for flow distortion by transducer shadowing. Bound.-Layer Meteorol. 155, 371–395. http://dx.doi.org/10.1007/s10546-015-0010-3.

Hung, W.T., Campbell, P.C., Moon, Z., Saylor, R., Kochendorfer, J., Lee, T.R., Massman, W., 2024. Evaluation of an in-canopy wind and wind adjustment factor model for wildfire spread applications across scales. J. Adv. Model. Earth Syst. 16, e2024MS004300. http://dx.doi.org/10.1029/2024MS004300.

ISFS, 2025. NSF NCAR/EOL integrated surface flux system (ISFS) guides. https://www.eol.ucar.edu/content/isfs-guides. (Accessed 11 July 2025).

Jerszurki, D., Couvreur, V., Maxwell, T., de Carvalho Ramos Silva, L., Matsumoto, N., Shackel, K., de Souza, J.L.M., Hopmans, J., 2017. Impact of root growth and hydraulic conductance on canopy carbon-water relations of young walnut trees (*Juglans regia* l.) under drought. Sci. Hortic. 226, 342–352. http://dx.doi.org/10.1016/j.scienta.2017.08.051.

Kasahara, A., Washington, W.M., 1967. NCAR global general circulation model of the atmosphere. Mon. Weather Rev. 95, 389–402. http://dx.doi.org/10.1175/1520-0493(1967)095<0389:NGGCMO>2.3.CO;2.

Kljun, N., Calanca, P., Rotach, M.W., Schmid, H.P., 2015. A simple two-dimensional parameterisation for Flux Footprint Prediction (FFP). Geosci. Model. Dev. 8, 3695–3713. http://dx.doi.org/10.5194/gmd-8-3695-2015.

Koven, C.D., Knox, R.G., Fisher, R.A., Chambers, J.Q., Christoffersen, B.O., Davies, S.J., Detto, M., Dietze, M.C., Faybishenko, B., Holm, J., Huang, M., Kovenock, M., Kueppers, L.M., Lemieux, G., Massoud, E., McDowell, N.G., Muller-Landau, H.C., Needham, J.F., Norby, R.J., Powell, T., Rogers, A., Serbin, S.P., Shuman, J.K., Swann, A.L.S., Varadharajan, C., Walker, A.P., Wright, S.J., Xu, C., 2020. Benchmarking and parameter sensitivity of physiological and vegetation dynamics using the Functionally Assembled Terrestrial Ecosystem Simulator (FATES) at Barro Colorado Island, Panama. Biogeosci. 17, 3017–3044. http://dx.doi.org/10.5194/bg-17-3017-2020.

Larson, V.E., Golaz, J.C., Cotton, W.R., 2002. Small-scale and mesoscale variability in cloudy boundary layers: Joint probability density functions. J. Atmos. Sci. 59, 3519–3539. http://dx.doi.org/10.1175/1520-0469(2002)059<3519:SSAMVI>2.0.CO;2.

Lawrence, D.M., Fisher, R.A., Koven, C.D., Oleson, K.W., Swenson, S.C., Bonan, G., Collier, N., Ghimire, B., van Kampenhout, L., Kennedy, D., Kluzek, E., Lawrence, P.J., Li, F., Li, H., Lombardozzi, D., Riley, W.J., Sacks, W.J., Shi, M., Vertenstein, M., Wieder, W.R., Xu, C., Ali, A.A., Badger, A.M., Bisht, G., van den Broeke, M., Brunke, M.A., Burns, S.P., Buzan, J., Clark, M., Craig, A., Dahlin, K., Drewniak, B., Fisher, J.B., Flanner, M., Fox, A.M., Gentine, P., Hoffman, F., Keppel-Aleks, G., Knox, R., Kumar, S., Lenaerts, J., Leung, L.R., Lipscomb, W.H., Lu, Y., Pandey, A., Pelletier, J.D., Perket, J., Randerson, J.T., Ricciuto, D.M., Sanderson, B.M., Slater, A., Subin, Z.M., Tang, J., Thomas, R.Q., Val Martin, M., Zeng, X., 2019. The community land model version 5: Description of new features, benchmarking, and impact of forcing uncertainty. J. Adv. Model. Earth Syst. 11, 4245–4287. http://dx.doi.org/10.1029/2018MS001583.

Lawrence, D., Fisher, R., Koven, C., Oleson, K., Swenson, S., Vertenstein, M., Andre, B., Bonan, G., Ghimire, B., Kampenhout, L.van., Kennedy, D., Kluzek, E., Knox, R., Lawrence, P., Li, F., Li, H., Lombardozzi, D., Lu, Y., Perket, J., Riley, W., Sacks, W., Shi, M., Wieder, W., Xu, C., Ali, A., Badger, A., Bisht, G., Broxton, P., Brunke, M., Buzan, J., Clark, M., Craig, T., Dahlin, K., Drewniak, B., Emmons, L., Fisher, J., Flanner, M., Gentine, P., Lenaerts, J., Levis, S., Leung, L.R., Lipscomb, W., Pelletier, J., Ricciuto, D.M., Sanderson, B., Shuman, J., Slater, A., Subin, Z., Tang, J., Twafik, A., Thomas, Q., Tilmes, S., Vitt, F., Zeng, X., 2018. Technical description of version 5.0 of the Community Land Model (CLM). https://escomp.github.io/CTSM/release-clm5.0/tech_note/index.html. (Accessed 11 July 2025).

Letestu, S., 1966. International Meteorological Tables. Technical Report, World Meteorological Organization, WMO-No. 188.TP.94.

Leuning, R., van Gorsel, E., Massman, W.J., Isaac, P.R., 2012. Reflections on the surface energy imbalance problem. Agric. For. Meteorol. 156, 65–74. http://dx.doi.org/10.1016/j.agrformet.2011.12.002.

Li, Y., Li, Z.L., Wu, H., Liu, X., Lian, X., Si, M., Li, J., Zhou, C., Tang, R., Duan, S., Zhao, W., Leng, P., Song, X., Shi, Q., Zhao, E., Gao, C., 2025. Observed different impacts of potential tree restoration on local surface and air temperature. Nat. Commun. 16, 2335. http://dx.doi.org/10.1038/s41467-025-57606-y.

Ma, Y., Liu, H., 2019. An advanced multiple-layer canopy model in the WRF model with large-eddy simulations to simulate canopy flows and scalar transport under different stability conditions. J. Adv. Model. Earth Syst. 11, 2330–2351. http://dx.doi.org/10.1029/2018MS001347.

Mahrt, L., Lee, X., Black, A., Neumann, H., Staebler, R.M., 2000. Nocturnal mixing in a forest subcanopy. Agric. Meteorol. 101, 67–78. http://dx.doi.org/10.1016/S0168-1923(99)00161-6.

Majasalmi, T., Bright, R.M., 2019. Evaluation of leaf-level optical properties employed in land surface models. Geosci. Model. Dev. 12, 3923–3938. http://dx.doi.org/10.5194/gmd-12-3923-2019.

Manabe, S., Smagorinsky, J., Strickler, R.F., 1965. Simulated climatology of a general circulation model with a hydrologic cycle. Mon. Weather Rev. 93, 769–798. http://dx.doi.org/10.1175/1520-0493(1965)093<0769:SCOAGC>2.3.CO;2.

Massman, W., Forthofer, J., Finney, M., 2017. An improved canopy wind model for predicting wind adjustment factors and wildland fire behavior. Can. J. For. Res. 47, 594–603. http://dx.doi.org/10.1139/cjfr-2016-0354.

Mauritsen, T., Svensson, G., 2007. Observations of stably stratified shear-driven atmospheric turbulence at low and high Richardson numbers. J. Atmos. Sci. 64, 645–655. http://dx.doi.org/10.1175/JAS3856.1.

Mayor, S.D., 2011. Observations of seven atmospheric density current fronts in Dixon, California. Agric. For. Meteorol. 139, 1338–1351. http://dx.doi.org/10.1175/2010MWR3374.1.

Mayor, S.D., 2017. Observations of microscale internal gravity waves in very stable atmospheric boundary layers over an orchard canopy. Agric. For. Meteorol. 244, 136–150. http://dx.doi.org/10.1016/j.agrformet.2017.05.014.

McElrone, A.J., Grant, J.A., Kluepfel, D.A., 2010. The role of tyloses in crown hydraulic failure of mature walnut trees afflicted by apoplexy disorder. Tree Physiol. 30, 761–772. http://dx.doi.org/10.1093/treephys/tpq026.

Meier, R., Davin, E.L., Swenson, S.C., Lawrence, D.M., Schwaab, J., 2019. Biomass heat storage dampens diurnal temperature variations in forests. Env. Res. Lett. 14, 084026. http://dx.doi.org/10.1088/1748-9326/ab2b4e.

Meinshausen, M., Vogel, E., Nauels, A., Lorbacher, K., Meinshausen, N., Etheridge, D.M., Fraser, P.J., Montzka, S.A., Rayner, P.J., Trudinger, C.M., Krummel, P.B., Beyerle, U., Canadell, J.G., Daniel, J.S., Enting, I.G., Law, R.M., Lunder, C.R., O'Doherty, S., Prinn, R.G., Reimann, S., Rubino, M., Velders, G.J.M., Vollmer, M.K., Wang, R.H.J., Weiss, R., 2017. Historical greenhouse gas concentrations for climate modelling (CMIP6). Geosci. Model. Dev. 10, 2057–2116. http://dx.doi.org/10.5194/gmd-10-2057-2017.

Mercado, L.M., Huntingford, C., Gash, J.H.C., Cox, P.M., Jogireddy, V., 2007. Improving the representation of radiation interception and photosynthesis for climate model applications. Tellus B 59, 553–565. http://dx.doi.org/10.1111/j.1600-0889.2007.00256.x.

Oncley, S.P., Foken, T., Vogt, R., Kohsiek, W., DeBruin, H.A.R., Bernhofer, C., Christen, A., van Gorsel, E., Grantz, D., Feigenwinter, C., Lehner, I., Liebethal, C., Liu, H., Mauder, M., Pitacco, A., Ribeiro, L., Weidinger, T., 2007. The energy balance experiment EBEX-2000. Part I: Overview and energy balance. Bound.-Layer Meteorol. 123, 1–28. http://dx.doi.org/10.1007/s10546-007-9161-1.

Pan, Y., Patton, E.G., 2017. On determining stationary periods within time series. J. Atmos. Ocean. Technol. 34, 2213–2232. http://dx.doi.org/10.1175/JTECH-D-17-0038.1.

Pan, Y., Patton, E.G., 2020. Determining stationary periods across multiple sensors: An application to observed canopy turbulence response to atmospheric stability. J. Atmos. Ocean. Technol. 37, 665–685. http://dx.doi.org/10.1175/JTECH-D-19-0135.1.

Pan, Y., Wray, S.C., Patton, E.G., 2025. Signals of non-turbulent motions caused by stable stratification in near-surface sonic-anemometer data. J. Atmos. Sci. 82, 1073–1091. http://dx.doi.org/10.1175/JAS-D-24-0070.1.

Patton, E.G., Horst, T.W., Sullivan, P.P., Lenschow, D.H., Oncley, S.P., Brown, W.O.J., Burns, S.P., Guenther, A.B., Held, A., Karl, T., Mayor, S.D., Rizzo, L.V., Spuler, S.M., Sun, J., Turnipseed, A.A., Allwine, E.J., Edburg, S.L., Lamb, B.K., Avissar, R., Calhoun, R.J., Kleissl, J., Massman, W.J., Paw, .K.T., Weil, J.C., 2011. The canopy horizontal array turbulence study. Bull. Amer. Meteorol. Soc. 92, 593–611. http://dx.doi.org/10.1175/2010BAMS2614.1.

Patton, E.G., Sullivan, P.P., Shaw, R.H., Finnigan, J.J., Weil, J.C., 2016. Atmospheric stability influences on coupled boundary layer and canopy turbulence. J. Atmos. Sci. 73, 1621–1647. http://dx.doi.org/10.1175/JAS-D-15-0068.1.

Pedruzo-Bagazgoitia, X., Patton, E.G., Moene, A.F., Ouwersloot, H.G., Gerken, T., Machado, L.A.T., Martin, S.T., Sörgel, M., Stoy, P.C., Yamasoe, M.A., Vilà-Guerau de Arellano, J., 2023. Investigating the diurnal radiative, turbulent, and biophysical processes in the Amazonian canopy-atmosphere interface by combining LES simulations and observations. J. Adv. Mod. Earth Syst. 15, e2022MS003210. http://dx.doi.org/10.1029/2022MS003210.

Raupach, M.R., Finnigan, J.J., 1988. Single-layer models of evaporation from plant canopies are incorrect but useful, whereas multilayer models are correct but useless: Discuss. Austral. J. Plant Physiol. 15, 705–716. http://dx.doi.org/10.1071/PP9880705.

Raupach, M.R., Finnigan, J.J., Brunet, Y., 1996. Coherent eddies and turbulence in vegetation canopies: The mixing-layer analogy. Bound.-Layer Meteorol. 78, 351–382. http://dx.doi.org/10.1007/BF00120941.

Roberts, J., Cabral, O.M.R., De Aguiar, L.F., 1990. Stomatal and boundary-layer conductances in an Amazonian terra firme rain forest. J. Appl. Ecol. 27, 336–353. http://dx.doi.org/10.2307/2403590.

Rosati, A., Metcalf, S., Buchner, R., Fulton, A., Lampinen, B., 2006. Tree water status and gas exchange in walnut under drought, high temperature and vapour pressure deficit. J. Hort. Sci. Biotech. 81, 415–420. http://dx.doi.org/10.1080/14620316.2006.11512082.

Ryder, J., Polcher, J., Peylin, P., Ottlé, C., Chen, Y., van Gorsel, E., Haverd, V., McGrath, M.J., Naudts, K., Otto, J., Valade, A., Luyssaert, S., 2016. A multi-layer land surface energy budget model for implicit coupling with global atmospheric simulations. Geosci. Model. Dev. 9, 223–245. http://dx.doi.org/10.5194/gmd-9-223-2016.

Schotanus, P., Nieuwstadt, F.T.M., Debruin, H.A.R., 1983. Temperature-measurement with a sonic anemometer and its application to heat and moisture fluxes. Bound.-Layer Meteorol. 26, 81–93. http://dx.doi.org/10.1007/BF00164332.

Sellers, P.J., Mintz, Y., Sud, Y.C., Dalcher, A., 1986. A simple biosphere model (SIB) for use within general circulation models. J. Atmos. Sci. 43, 505–531. http://dx.doi.org/10.1175/1520-0469(1986)043<0505:ASBMFU>2.0.CO;2.

Shapkalijevski, M., Moene, A.F., Ouwersloot, H.G., Patton, E.G., Vilà-Guerau de Arellano, J., 2016. Influence of canopy seasonal changes on turbulence parameterization within the roughness sublayer over an orchard canopy. J. Appl. Meteorol. Clim. 55, 1391–1407. http://dx.doi.org/10.1175/JAMC-D-15-0205.1.

Shapkalijevski, M.M., Ouwersloot, H.G., Moene, A.F., Vilà-Guerau de Arellano, J., 2017. Integrating canopy and large-scale effects in the convective boundary-layer dynamics during the CHATS experiment. Atmos. Chem. Phys. 17, 1624–1641. http://dx.doi.org/10.5194/acp-17-1623-2017.

Shawcroft, R., Lemon, E., Allen, L., Stewart, D., Jensen, S., 1974. The soil-plant-atmosphere model and some of its predictions. Agric. Meteorol. 14, 287–307. http://dx.doi.org/10.1016/0002-1571(74)90025-9.

Simpson, I.R., Garcia, R.R., Bacmeister, J.T., Lauritzen, P.H., Hannay, C., Medeiros, B., Caron, J., Danabasoglu, G., Herrington, A., Jablonowski, C., Marsh, D., Neale, R.B., Polvani, L.M., Richter, J.H., Rosenbloom, N., Tilmes, S., 2025. The path toward vertical grid options for the Community Atmosphere Model Version 7: The impact of vertical resolution on the QBO and tropical waves. J. Adv. Model. Earth Syst. 17, e2025MS004957. http://dx.doi.org/10.1029/2025MS004957.

Smallman, T.L., Moncrieff, J.B., Williams, M., 2013. WRFv3.2-SPAv2: development and validation of a coupled ecosystem–atmosphere model, scaling from surface fluxes of CO_2 and energy to atmospheric profiles. Geosci. Model. Dev. 6, 1079–1093. http://dx.doi.org/10.5194/gmd-6-1079-2013.

Stöckli, R., Lawrence, D.M., Niu, G.Y., Oleson, K.W., Thornton, P.E., Yang, Z.L., Bonan, G.B., Denning, A.S., Running, S.W., 2008. Use of FLUXNET in the community land model development. J. Geophys. Res.: Biogeosci. 113, G01025. http://dx.doi.org/10.1029/2007JG000562.

Sun, S.J., Meng, P., Zhang, J.S., Wan, X., 2011. Variation in soil water uptake and its effect on plant water status in *Juglans regia* L. during dry and wet seasons. Tree Physiol. 31, 1378–1389. http://dx.doi.org/10.1093/treephys/tpr116.

Swenson, S.C., Burns, S.P., Lawrence, D.M., 2019. The impact of biomass heat storage on the canopy energy balance and atmospheric stability in the Community Land Model. J. Adv. Model. Earth Syst. 11, 83–98. http://dx.doi.org/10.1029/2018MS001476.

Thom, A.S., 1975. Momentum, mass and heat exchange of plant communities. In: Monteith, J.L. (Ed.), Vegetation and the Atmosphere: 1. Principles. Academic Press, New York, NY, pp. 57–109.

Turnipseed, A.A., Blanken, P.D., Anderson, D.E., Monson, R.K., 2002. Energy budget above a high-elevation subalpine forest in complex topography. Agric. For. Meteorol. 110, 177–201. http://dx.doi.org/10.1016/S0168-1923(01)00290-8.

Tyree, M.T., Cochard, H., Cruiziat, P., Sinclair, B., Ameglio, T., 1993. Drought-induced leaf shedding in walnut: evidence for vulnerability segmentation. Plant Cell Env. 16, 879–882. http://dx.doi.org/10.1111/j.1365-3040.1993.tb00511.x.

Tyree, M.T., Yang, S., Cruiziat, P., Sinclair, B., 1994. Novel methods of measuring hydraulic conductivity of tree root systems and interpretation using AMAIZED (a maize-root dynamic model for water and solute transport). Plant Physiol. 104, 189–199. http://dx.doi.org/10.1104/pp.104.1.189.

van Dijk, A., Kohsiek, W., de Bruin, H.A.R., 2003. Oxygen sensitivity of krypton and lyman-α hygrometers. J. Atmos. Ocean. Technol. 20, 143–151. http://dx.doi.org/10.1175/1520-0426(2003)020<0143:OSOKAL>2.0.CO;2.

Vermeuel, M.P., Millet, D.B., Farmer, D.K., Ganzeveld, L.N., Visser, A.J., Alwe, H.D., Bertram, T.H., Cleary, P.A., Desai, A.R., Helmig, D., Kavassalis, S.C., Link, M.F., Pothier, M.A., Riches, M., Wang, W., Williams, S., 2024. A vertically resolved canopy improves chemical transport model predictions of ozone deposition to north temperate forests. J. Geophys. Res.: Atmos. 129, e2024JD042092. http://dx.doi.org/10.1029/2024JD042092.

Waggoner, P.E., Reifsnyder, W.E., 1968. Simulation of the temperature, humidity and evaporation profiles in a leaf canopy. J. Appl. Meteorol. 7, 400–409. http://dx.doi.org/10.1175/1520-0450(1968)007<0400:SOTTHA>2.0.CO;2.

Webb, E.K., Pearman, G.I., Leuning, R., 1980. Correction of flux measurements for density effects due to heat and water vapour transfer. Q. J. R. Meteorol. Soc. 106, 85–100. http://dx.doi.org/10.1002/qj.49710644707.

Wilczak, J.M., Oncley, S.P., Stage, S.A., 2001. Sonic anemometer tilt correction algorithms. Bound.-Layer Meteorol. 99, 127–150. http://dx.doi.org/10.1023/A:1018966204465.

Williams, M., Rastetter, E.B., Fernandes, D.N., Goulden, M.L., Wofsy, S.C., Shaver, G.R., Melillo, J.M., Munger, J.W., Fan, S.M., Nadelhoffer, K.J., 1996. Modelling the soil-plant-atmosphere continuum in a *Quercus–Acer* stand at harvard forest: the regulation of stomatal conductance by light, nitrogen and soil/plant hydraulic properties. Plant Cell Env. 19, 911–927. http://dx.doi.org/10.1111/j.1365-3040.1996.tb00456.x.

Wiltshire, A.J., Duran Rojas, M.C., Edwards, J.M., Gedney, N., Harper, A.B., Hartley, A.J., Hendry, M.A., Robertson, E., Smout-Day, K., 2020. JULES-GL7: the Global land configuration of the joint UK land environment simulator version 7.0 and 7.2. Geosci. Model. Dev. 13, 483–505. http://dx.doi.org/10.5194/gmd-13-483-2020.

Wozniak, M.C., Bonan, G.B., Keppel-Aleks, G., Steiner, A.L., 2020. Influence of vertical heterogeneities in the canopy microenvironment on interannual variability of carbon uptake in temperate deciduous forests. J. Geophys. Res.: Biogeosci. 125, e2020JG005658. http://dx.doi.org/10.1029/2020JG005658.

Xu, L., Pyles, R.D., Paw U, K.T., Chen, S.H., Monier, E., 2014. Coupling the high-complexity land surface model ACASA to the mesoscale model WRF. Geosci. Model. Dev. 7, 2917–2932. http://dx.doi.org/10.5194/gmd-7-2917-2014.

Zaremba, L.L., Carroll, J.J., 1999. Summer wind flow regimes over the Sacramento Valley. J. Appl. Meteorol. 38, 1463–1473. http://dx.doi.org/10.1175/1520-0450(1999)038<1463:SWFROT>2.0.CO;2.

Zlotnick, O.B., Musselman, K.N., Levy, O., 2024. Deforestation poses deleterious effects to tree-climbing species under climate change. Nat. Clim. Chang. 14, 289–295. http://dx.doi.org/10.1038/s41558-024-01939-x.